

Variation of sediment supply by periglacial debris flows at Zelunglung in the eastern syntaxis of Himalayas since the 1950 Assam Earthquake

Kaiheng Hu^{1,2}, Hao Li^{1,2,3}, Shuang Liu^{1,2}, Li Wei^{1,2}, Xiaopeng Zhang^{1,2,3}, Limin Zhang⁴, Bo Zhang^{1,2}, Manish Raj Gouli^{1,2,3}

¹Key Laboratory of Mountain Hazards and Earth Surface Processes, Chinese Academy of Sciences, Chengdu, 610041, China

²Institute of Mountain Hazards and Environment, Chinese Academy of Sciences, Chengdu, 610041, China

³University of Chinese Academy of Sciences, Beijing 100049, China

⁴Department of Civil and Environmental Engineering, The Hong Kong University of Science and Technology, Clear Water Bay, Hong Kong, China

Correspondence: Kaiheng Hu (khhu@imde.ac.cn)

ABSTRACT. Periglacial debris flows boosted by strong earthquakes or climatic warming in alpine mountains play a crucial role in sediment delivery from hillslopes and downslope channels into rivers. Rapid and massive sediment supply to rivers by the debris flows has profoundly influenced the evolution of the alpine landscape. Nonetheless, there is a dearth of knowledge concerning the roles tectonic and climatic factors played in the intensified sediment erosion and transportation. In order to increase our awareness of the mass wasting processes and glacier changes, five debris flows that occurred at the Zelunglung catchment of the eastern syntaxis of the Himalayas since 1950 Assam earthquake are investigated in detail by field surveys and long-term remote sensing interpretation. Long-term seismic and meteorological data indicate that the four events of 1950-1984 were the legacies of the earthquake, and recent warming events drove the 2020 event. The transported sediment volume indexed with a non-vegetated area on the alluvial fan reduced by 91% to a stable low level nearly 40 years after 1950. It is reasonable to hypothesize that tectonic and climatic factors alternately drive the sediment supplies caused by the debris flows. High concentrations of coarse grains, intense erosion, and extreme impact force of the 2020 debris flow raised concerns about the impacts of such excess sediment inputs on the downstream river evolution and infrastructure safety. In regard to the hydrometeorological conditions of the main river, the time to evacuate the transported coarse sediments is approximately two orders of magnitude of the recurrence period of periglacial debris flows.

1 Introduction

Glacier-related hazards are widely developed in alpine regions around the world, such as the Alps, Himalayas, Caucasus, Tianshan, and Andes (Richardson and Reynolds, 2000; Anacona et al., 2015; Shen et al., 2013; Petrakov et al., 2007; Huggel et al., 2004). These hazards, including ice/rock avalanches, periglacial debris flows, glacial lake outburst floods (GLOFs), and dammed lakes, have caused huge economic and human losses in the high mountains and their surrounding area (Yu et al.,

2021; Tian et al., 2017; Bajracharya and Mool, 2009; Hu et al., 2019). Earthquakes, geothermal heating, climate warming, rainfall, and meltwater all trigger glacier-related hazards (Huggel, 2004; Haeberli et al., 2014). Especially in the context of climate change (rising temperatures and increased extreme precipitation events), the high-altitude regions such as European mountains, high-mountain Asia, and the Andes are undergoing rapid deglaciation that increases the magnitude and frequency of ice/rock avalanches and low-angle glacier detachments accordingly (Anaconda et al., 2015; Krautblatter et al., 2013).

In recent years, the Earthquakes, climate warming, geothermal heating, rainfall, and meltwater all directly trigger glacier-related hazards (Huggel, 2004; Haeberli et al., 2014). The Himalayan mountains, which are tectonically active and sensitive to climate change, have experienced many glacier-related disasters triggered by large-magnitude earthquakes or climate warming-driven disasters in recent years. The increased glacier-related disasters have profound hydrogeomorphic and socio-economic impacts on the high-altitude and surrounding regions, including sediment yield and transportation, alpine landscape evolution, river management, food and water security, hydropower utilization, and infrastructure construction (Evans and Clague, 1994; Kääb et al., 2021). For example, on 25 April 2015, a disastrous ice-rock collapse was triggered by the Gorkha earthquake and killed or left missing at least 350 people in the Langtang Valley of central Nepal (Kargel et al., 2016). From 2017 to 2018, several ice-rock avalanches in the Sedongpu catchment of Milin County, Tibet Autonomous Region (TAR), China triggered large-scale glacial debris flow events that blocked the Yarlung Tsangpo River twice (Li et al., 2022; Hu et al., 2019; Jia et al., 2019). On 7 February 2021, about $27 \times 10^6 \text{ m}^3$ of rock and ice collapsed and quickly transformed into a debris flow in Chamoli, Uttarakhand region of India, which killed more than 200 people and severely damaged two hydropower projects (Shugar et al., 2021). The increased disasters have profound hydrogeomorphic and socio-economic impacts on the high-altitude and surrounding regions, including sediment yield and transportation, alpine landscape evolution, river management, food and water security, hydropower utilization, and infrastructure construction (Evans and Clague, 1994; Kääb et al., 2021). These disasters seriously threaten the safety of life and property of local and downstream residents, leading to the challenges of transboundary hazards and international collaboration.

Periglacial debris flows transformed from When upstream ice-rock avalanches, glacier surges, or GLOFs driven by earthquake or climatic events are accompanied by ice melting, mass mixing, and bed entrainment in the channelized propagation, they often transform into periglacial debris flows. The debris flows are a major agent of sediment evacuation from steep lands to rivers in high-altitude mountains at low-order catchments. The volume of ice loss and sediment transportation via periglacial debris flows is huge and poses long-term effects on the high mountain environment. The Institute of Mountain Hazards and Environment, Chinese Academy of Sciences (IMHE, CAS) reported that a total volume of 200 Mm^3 of sediment transported into an upstream tributary of the Brahmaputra River by periglacial debris flows of the Guxiang catchment in southeastern Tibet from 1953 to 1999 (Wang et al., 2022). The ice-rock avalanches of the Sedongpu in October 2018 delivered about 33.2 Mm^3 of sediment into the Yarlung Tsangpo River (Hu et al., 2019). The total mass loss caused by glacier-rock avalanches in Sedongpu between 2014 and 2018 reached $> 70 \text{ Mm}^3$ of glacier and rock and $> 150 \text{ Mm}^3$ of moraine deposits (Li et al., 2022). Furthermore, after the glacier detachment of the Sedongpu in 2018, a huge volume of $\sim 335 \text{ Mm}^3$ was eroded from its glacier

bed and transported into the Yarlung Tsangpo (Kääb and Girod, 2023). Sudden enormous sediment inputs greatly influence sediment transport capacity, knickpoint formation, river water quality, downstream floods, and delta progradation. The 2021 Chamoli event resulted in extremely suspended sediment as 80 times high as the permissible level in the Ganga River, ~900 km from the source (Shugar et al., 2021). Sediment fluxes have increased two- to eight-fold in many glacierized and periglacierized basins between the 1950s and 2010s (Zhang et al., 2022a). ~~However~~Until now, most of previous studies have focused on the residence time and transport of earthquake-triggered landslide sediment at an orogenic scale in no-glacierized environments (Dadson et al., 2004; Dai et al., 2021; Parker et al., 2011; Wang et al., 2015). Little attentions are paid on the sediment evacuation progress by post-seismic debris flows at a catchment in glacierized environments disturbed by a strong earthquake-owing to relatively low likelihood of debris flows and absence of long-term site-specific data. However, little is known about the roles played by the extreme hazards play in incrementing sediment erosion, and transportation, also the roles played by and the control of the hazards between tectonic and climatic factors in controlling hazards.

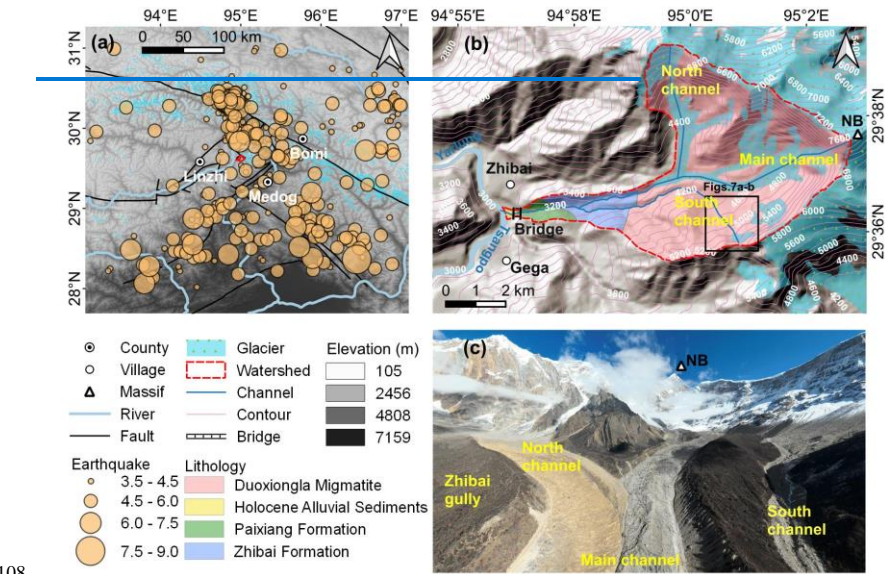
~~12. Second, it is not made clear in the following text how that knowledge gap is addressed by the study. Questions that would be good to answer in the introduction are: Why was that particular study area chosen? How do the approaches advance the gap that you are proposing? In the discussion or conclusion, you can also come back to that point. Long-term remote sensing imagery.]~~

In order to investigate the long-term effects of earthquakes on sediment evacuation in a glaciated catchment, ~~In this paper, This paper investigates glacier changes and associated debris flows in the~~ Zelunglung catchment, a tributary of the Yarlung Tsangpo river in southeastern Tibet ~~that has large areas of temperate glaciers and disturbed intensely by thea Ms 8.5 earthquake in 1950.is, relatively well documented and has long term remote sensing imagery for interpreting glacier changes and associated debris flows~~ is chosen as our study case. The catchment has long-term remote sensing imagery for interpreting glacier changes and associated debris flows and relatively well-documented records of ~~had experienced~~ at least four historical periglacial debris flows in 1950, 1968, 1972, and 1984 since the 1950 Assam earthquake (Zhang, 1992; Zhang and Shen, 2011). ~~The catchment has is relatively well documented and has long term remote sensing imagery for interpreting This paper investigates glacier changes and associated debris flows in. Four historical periglacial debris flows occurred in this catchment in 1950, 1968, 1972, and 1984 (Zhang, 1992; Zhang and Shen, 2011).~~ The most recent debris-flow event occurred on 10 September 2020, triggered by a small-scale ice-rock avalanche. It is believed that historical earthquakes and ongoing climate warming drive these events. Field surveys were carried out before and after the 2020 event, including three periods of aerial photography on 8 September, 11 September 2020, and December 21, 2022, with DJI Unmanned Aerial Vehicle (UAV). Dynamic process and sediment characteristics of the 2020 event were examined with the details of aerial photos and field measurements. The Zelunglung's glacier and alluviation fan changes were interpreted with high-resolution optical remote sensing images from 1969 to 2022. The non-vegetated area of the alluvial fan was used as an index to reflect the variation of sediment supply caused by the periglacial debris flows. Integrating with historical data of neighboring earthquakes, temperature, and precipitation, we demonstrate the trend of periglacial debris flows in different periods. This case study is

97 helpful for a better understanding of the controlling factors and sediment transportation of periglacial debris flows in High
98 Mountain Asia (HMA).

99 **2 Study area**

100 The Zelunglung catchment (ZLL) (94°56'13.4"E, 29°36'25.6"N) at Zhibai Village in the China's TAR is a tributary on the
101 right bank of the lower Yarlung Tsangpo River, originating from the west side of Namche Barwa massif (7782 m) in the
102 easternmost part of the Himalayas. The main stream flows westward into the Yarlung Tsangpo at an elevation of 2810 m, with
103 a local relief of 4972 m (Fig. 1ab). It has a drainage area of 41.21 km² with a 17.9 km² glacier area. High lateral moraines on
104 both sides of the main glacier divide the drainage network into the main channel, south branch, and north branch (Fig. 1bc).
105 The south branch, with a total length of 9.8 km and an average gradient of 275%, originates from the southern cliff at an
106 elevation of ~5900 m. Hanging glaciers on the ridge and freeze-thawing in the cold region make the study area prone to ice
107 and rock avalanches (Fig. 1e1d).



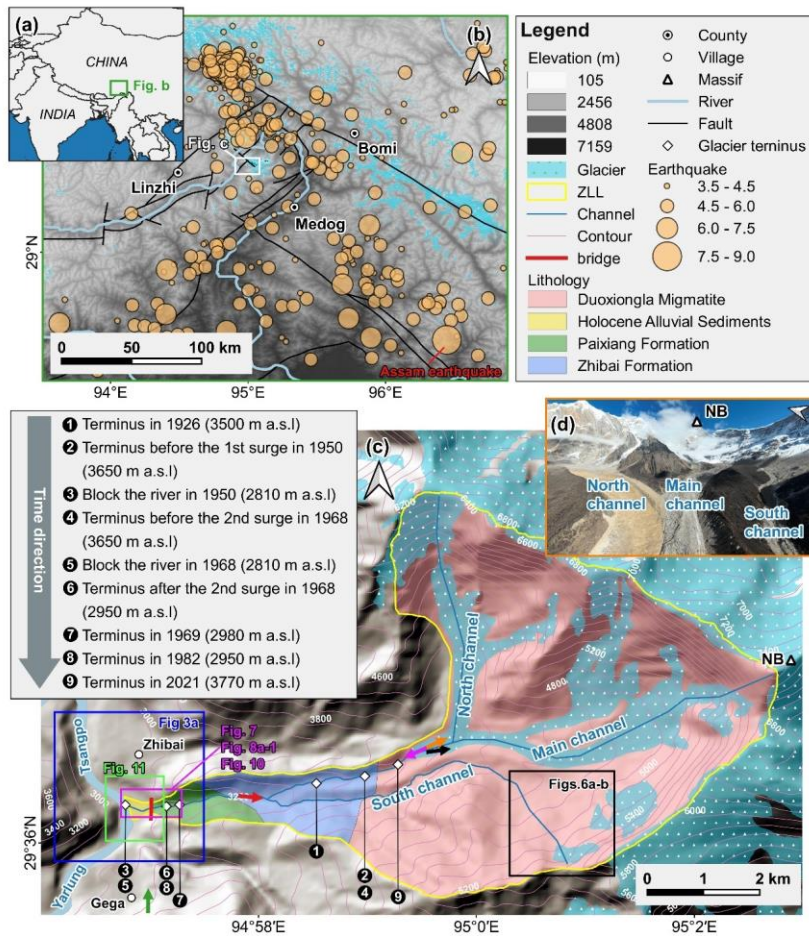
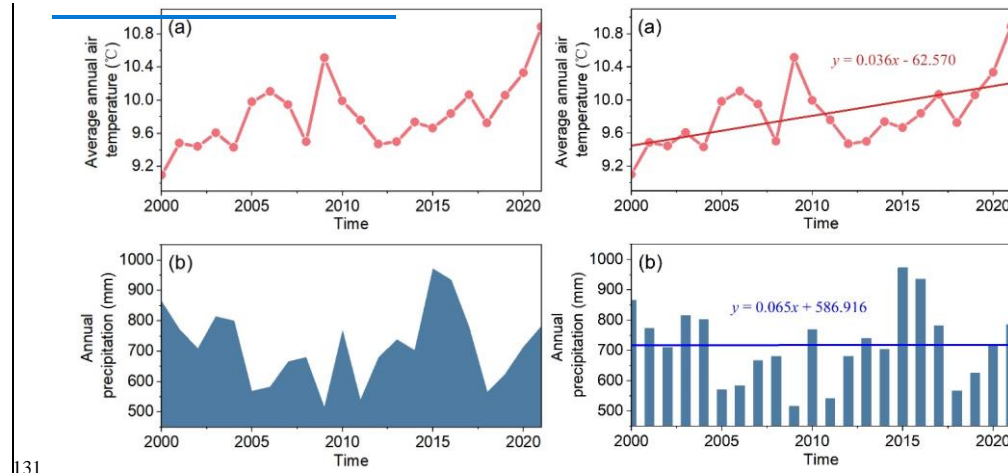


Figure 1: (a) Regional overview map of southeastern Tibet. (b) Regional settings and historical earthquakes of southeastern Tibet. (c) Topographic and geological and glacier terminus change maps of the Zelunglung catchment (the lithology refers to (Zhang and Shen, 2011)). The orange, rose-red, green, black and red coloured arrows represent the view angle direction of figures 1d, 4, 5, 6c and 6d. (d) Aerial photo of the Zelunglung glacier and channels on December 21, 2022 (NB denotes the Namche Barwa massif).

The regional tectonic units are the Lhasa terrane, the Indus-Yarlung Tsangpo suture, and the eastern syntaxis of the Himalayas from north to south (Hu et al., 2021). The catchment lies in the eastern syntaxis, which is uplifting at a rate of 5-10

116 mm/a (Ding et al., 2001). The exposed stratum in the Zelunglung is known as the Namche Barwa Group complex, which is
 117 composed of Duoxiongla migmatite, Zhibai group, and Paixiang group gneiss. The Quaternary deposits consist of Holocene
 118 alluvium at its outlet, thick layers of glacial till, and glacio-fluvial accumulation, especially hundreds of meters of huge thick
 119 moraine layers with large boulders accumulated on both sides of the main channel (Fig. 4b1c) (Han and Feng, 2018; Zhang
 120 and Shen, 2011). Many active faults are distributed around the study area, such as the Aniqiao-Medog Fault to the east, which
 121 is considered the seismogenic fault of the 1950 Ms=8.5 Assam earthquake, NW-SE Xixingla fault that is the seismogenic fault
 122 of the 2017 Ms=6.9 Milin earthquake, and Daduka Fault across the Zelunglung downstream (Hu et al., 2019). Neotectonic
 123 movement makes this area highly susceptible to intense and frequent earthquakes.

124 This catchment lies in the rain shadow area of Mt. Namche Barwa, and its precipitation is controlled by the Indian Ocean's
 125 humid monsoon through the Yarlung Tsangpo Gorge. The climate has a strong vertical difference: semi-humid climate zone
 126 beneath 3200 m, cold temperate climate zone between 3200-4000 m, and cold climate zone above 4000 m. According to the
 127 data recorded at the Linzhi meteorological station 46.2 km west of the Zelunglung, the annual air temperature with a mean
 128 value of 9.8 °C increases at an average rate of 0.36 °C/10a from 2000 to 2021, which is much higher than the global average
 129 (Chen et al., 2015). Meanwhile, the annual precipitation ranges from 514 mm to 972 mm and increases at an average rate of
 130 0.65 mm/10a (Fig. 2).



131
 132 Figure 2: Annual temperature and precipitation data from 2000 to 2021 at Linzhi Meteorological Station. (Data source:
 133 <https://www.ncei.noaa.gov/maps/annual/>).

134 The ZLL basin, with its unique geographical and climatic conditions, has been a cradle for the extensive proliferation of
135 glaciers and a hotbed of frequent glacial activity throughout geological time. The Zelunglung has experienced at least three
136 glaciations in the Last Glacial Maximum (LGM), Neoglaciation, and Late Holocene (Hu et al., 2020). The LGM moraine
137 extended into the Yarlung Tsangpo and dammed the river (David et al., 2004; Huang et al., 2014; Zhu et al., 2012; Liu et al.,
138 2006). The glacier surges/debris flows - dammed lake - outburst flood disaster events since the last glacial period also had an
139 important impact on the landform and paleogeographical environment of the Yarlung Tsangpo Valley (Wang et al., 2021).
140 The modern glaciers in this area are strongly influenced by the Indian monsoon and are highly sensitive to climate change.
141 Hence, the Zelunglung glacier has advanced and retreated many times since the last century. The high instability and rapid
142 changes of the glacier result in several glacier surges or calving events. As shown in Fig. 31c, the glacier snout was 3500 m
143 a.s.l in 1926 (Ward, 1926). Since the 1950s, the Zelunglung glacier has experienced three surges or rapid advances (Zhang,
144 1985, 1992). The first surge occurred on August 15, 1950. Following the 1950 Assam earthquake, the terminus of Zelunglung
145 Glacier advanced from 3650 m a.s.l to the Yarlung Tsangpo at 2810 m a.s.l with a horizontal displacement of up to 4.5 km.
146 This event destroyed the Zhibai Village completely at the mouth of the Zhibai gully, killed 98 people, and formed an ice dam
147 as high as tens of meters in the main river. The second surge occurred one afternoon in August or September of 1968 (July
148 1968, Tibetan calendar) when it was sunny (Zhang, 1992, 1985). The advance also resulted in a temporary ice dam in the
149 Yarlung Tsangpo and deposited a glacial boulder of 4.0×5.0×5.5 m upstream of the dam (Zhang, 1985). It is worth noting that
150 the position of the ice tongue before the second glacier surge has returned to the position before the first surge (3650 m a.s.l),
151 and the highest speed of the two glacier surges was up to 1.5 km/d. After the second surge, the main glacier split into 6 segments
152 due to differential ablation, and the terminus of the lowest segment of the glacier was at 2950 m a.s.l. The terminus of the
153 lowest segment was about 2980 m a.s.l in 1969 as shown by the Corona reconnaissance satellite images (Kääb et al., 2021).
154 The terminus of the lowest part of the glacier had probably been at 2950 m a.s.l before 13 April 1984 when an ice mass of
155 80000 m³ detached at 3700 m a.s.l and traveled horizontally 150 m, which was the third rapid advance of the Zelunglung
156 glacier (Zhang, 1992). After that, no glacier surges or detachments were recorded, but small-scale mountain torrent or debris
157 flows occurred almost yearly (Zhang and Shen, 2011). At present, the glacier terminus is about 3770 m a.s.l.

159 3 Data and methodology

160 3.1 Data sources

161 We collected a total of 30 different remote sensing images from various sources dating back to 1969, with resolutions ranging
162 from 1m to 15m (Table 1). The 1969 Keyhole image refers to Kääb et al. (2021) and the other images before 1982 were
163 sourced from the Keyhole reconnaissance satellites (<https://earthexplorer.usgs.gov/>), originally serving as the primary data
164 source for the United States Department of Defence and intelligence agencies for Earth imaging. These high-resolution images

域代码已更改

域代码已更改

设置了格式: 字体:加粗

域代码已更改

设置了格式: 字体:(中文)+中文正文(宋体)

带格式的: 正文

设置了格式: 字体颜色: 蓝色

域代码已更改

165 provide valuable visible data in the era without commercial satellite imagery. Images from 1988 to 2007 originated from the
166 Centre National d’Études Spatiales (CNES) SPOT series data (<https://regards.cnes.fr/user/swh/modules/60>). Images from 2009
167 are sourced from the RapidEye series and Planet satellites (<https://account.planet.com/>), which are known for their short revisit
168 periods and high resolution. To comprehensively document the historical debris flow activity in Zelunglung, we diligently
169 chose images captured after every rainy season (October to December) whenever feasible. Due to high cloud cover in the study
170 area and limited availability of image resources, we substituted images from the following year before May for specific periods
171 with significant image data gaps (e.g., before 2000) for those of the missing year ([Li et al., 2017](#)). Although the Landsat satellite
172 series may offer more continuous observational records, their relatively coarse resolution makes them unsuitable for our study
173 area.

174 **Table 1: Data sources of the satellite images used in this study.**

No.	Date	Data sources	Resolution (m)
1	1969	Keyhole	5
2	1972/2/28	Keyhole	1
3	1973/3/26	Keyhole	1
4	1975/12/21	Keyhole	4
5	1979/4/10	Keyhole	1
6	1982/10/15	Keyhole	1
7	1988/2/20	Spot1	15
8	1989/12/1	Spot1	15
9	1990/12/21	Spot2	12
10	1991/11/25	Spot3	12
11	2000/11/17	Spot4	10
12	2002/12/5	Spot5	6
13	2004/12/28	Spot5	6
14	2005/10/10	Spot5	6
15	2006/12/21	Spot5	6
16	2007/11/29	Spot5	6
17	2009/12/22	RapidEye	5
18	2010/12/15	RapidEye	5
19	2011/11/23	RapidEye	5
20	2012/12/15	RapidEye	5
21	2013/12/7	RapidEye	5
22	2014/12/13	RapidEye	5

23	2015/12/6	RapidEye	5
24	2016/12/13	Planet	3
25	2017/12/11	Planet	5
26	2018/12/13	Planet	3
27	2019/12/7	Planet	3
28	2020/12/10	Planet	3
29	2021/12/12	Planet	3
30	2022/12/10	Planet	3

175 **3.2 Field surveys-Methodology**

176 This study utilizes a combination of field surveys, aerial drone photography, and satellite imagery analysis to investigate debris
177 flow events in the Zelunglung region. The historical records of the four debris flows have no volume data. High-resolution
178 orthoimages and digital surface models are generated to assess terrain changes, while non-vegetated area (NVA) serves as a
179 proxy for sediment volume for time series analysis. The integration of these methods offers a detailed insight into the debris
180 flow history and its influencing factors.

181 **3.2.1 Field surveys**

182 We conducted three field surveys in the Zelunglung between 2020 - 2022. During the initial two first-survey, we conducted
183 two aerial drone photography works on September 9 and 11, 2020, using DJI MAVIC 2. High-resolution orthoimages and
184 digital surface models (DSM) for the channel and fan areas of Zelunglung were generated from the aerial photos. Additionally,
185 we measured downstream channel cross-sectional morphology, debris flow particle characteristics, and the extent of damage
186 to the Zhibai Bridge, and sampled debris flow materials with size < 100 mm on the accumulation fan in the second survey. In
187 2021, we conducted a follow-up field survey at the same site. A full 3D view of the Zelunglung was captured with an unmanned
188 aerial vehicle (UAV) in the third survey on December 21, 2022, a sunny winter day (Fig. 1e1d).

189 **3.3-2.2 MethodologyNVA interpretation**

190 The inundation of debris flow on the alluvial fan often destroys vegetation cover and causes the affected area to
191 desertifydesertification in a few years. Generally, the non-vegetated area (NVA) depends on the flow magnitude. So, the non-
192 vegetated area of the alluvial fan shortly after a glacial debris flow can serve as a proxy of the volume of transported sediment.
193 It should be noted that distinguishing fresh debris flow deposits on an alluvial fan from pre-existing exposed surfaces in the
194 surrounding area is challenging in satellite images due to minimal color differences. Additionally, due to the slow vegetation
195 recovery rate in high-altitude regions, our interpretation area likely includes exposed areas one year or several years before an
196 event. Therefore, the NVA has some uncertainties in representing the real magnitude of the debris flows.

带格式的: 标题 3

设置了格式: 字体: (中文) + 中文正文 (宋体)
带格式的: 标题 3

197 We employed a visual interpretation approach to delineate non-vegetated areas within the Zelunglung's alluvial fan.
198 Identifying the non-vegetated area is primarily based on differences in color, hue, texture, and shading between vegetated and
199 unvegetated regions. The Keyhole black and white photos and the SPOT single-band black and white images show distinct
200 tonal differences between vegetated and unvegetated areas. In the true-color images obtained from RapidEye and Planet, the
201 boundaries of NVAs are highly conspicuous. The Zelunglung interpretation zone is limited to the region between the two
202 adjacent confluences of its upstream and downstream catchments with the main river.
203 Due to potential misalignment between remote sensing images from different sources, image matching is performed before
204 manual delineation of the non-vegetated areas (Cui et al., 2022). To eliminate the errors of geospatial locations of the images
205 from different sources, we used the 2020 Planet image as the reference image and selected ground control points with clear
206 markers on this image, such as road junctions, rivers, and typical topographic points. Third-order polynomial transformation
207 is applied to match the images from other sources accurately with the 2020 image, ensuring a positional error of less than 20
208 m relative to the reference image. The original Keyhole images without geographical coordinates and projection system
209 information are georeferenced with the 2020 Planet image with the ground control points. We assume that the visual
210 interpretation error of non-vegetated areas is approximately one grid cell on either side of the boundary. Moreover, we verified
211 the interpretation results of the remote sensing images with the UAV orthoimages.

212 3.2.3 Drone image interpretation

213 We employed Pix4DMapper and Arcmap10.8 to deal with the UAV digital orthophoto maps (DOMs) and digital surface
214 models (DSMs) generation and DSMs differencing. Since we did not deploy ground control points (GCPs) during drone
215 photography, we generated DSM and DOM of September 9 in Pix4DMapper, and then selected 20 relatively stable points that
216 were not affected by debris flow events as GCPs in Arcmap with DOM of September 9 as reference. These control points were
217 then used in Pix4DMapper to generate the September 11 DSM and DOM. Then the DSMs of difference (DoD) differencing
218 was conducted in Arcmap. To determine the uncertainty for our DoD differencing result we follow methods outlined in Shugar
219 et al. (2021). We identified a series of fifteen stable areas on old debris flow terraces adjacent to the valley floor (Mainly roads
220 and unseeded farmlands) and retrieved the standard deviation of DoD values within these areas and used these to estimate a
221 two-sigma DoD uncertainty. The uncertainty was ± 0.493 m.

222 Utilizing post-event drone orthoimages-DOM captured in on September 11 2020, we visually interpreted the distribution of
223 particles from the downstream channel to the depositional fan on Arcmap10.8. High resolution and accurate color
224 representation of the drone aerial images enable us to reliably identify coarse particles (>50 cm). The interpretation results
225 were compared with measurements obtained with a caliper during the 2022 field survey.

带格式的: 标题 3

226 **4 Glacier changes and debris****Debris-flow events and Sediment characteristics**

227 **4.1 Rapid glacier changes**

228 The Zelonglung has experienced at least three glaciations in the Last Glacial Maximum (LGM), Neoglaciation, and Late

229 Holocene (Hu et al., 2020). The LGM moraine extended into the Yarlung Tsangpo and dammed the river (David et al., 2004;

230 Huang et al., 2014; Zhu et al., 2012; Liu et al., 2006). The glacier surges/debris flows – dammed lake – outburst flood disaster

231 events since the last glacial period also had an important impact on the landform and paleogeographical environment of the

232 Yarlung Tsangpo Valley (Wang et al., 2021).

233 The modern glaciers in this area are strongly influenced by the Indian monsoon and are highly sensitive to climate change.

234 Hence, the Zelonglung glacier has advanced and retreated many times since the last century. The high instability and rapid

235 changes of the glacier result in several glacier surges or calving events. As shown in Fig. 3, the glacier snout was 3500 m a.s.l

236 in 1926 (Ward, 1926). Since the 1950s, the Zelonglung glacier has experienced three surges or rapid advances (Zhang, 1985;

237 1992). The first surge occurred on August 15, 1950. Following the 1950 Assam earthquake, the terminus of Zelonglung Glacier

238 advanced from 3650 m a.s.l to the Yarlung Tsangpo at 2810 m a.s.l with a horizontal displacement of up to 4.5 km. This event

239 destroyed the Zhibai Village completely at the mouth of the Zhibai gully, killed 98 people, and formed an ice dam as high as

240 tens of meters in the main river. The second surge occurred one afternoon in August or September of 1968 (July 1968, Tibetan

241 calendar) when it was sunny (Zhang, 1992, 1985). The advance also resulted in a temporary ice dam in the Yarlung Tsangpo

242 and deposited a glacial boulder of 4.0×5.0×5.5 m upstream of the dam (Zhang, 1985). It is worth noting that the position of

243 the ice tongue before the second glacier surge has returned to the position before the first surge (3650 m a.s.l), and the highest

244 speed of the two glacier surges was up to 1.5 km/d. After the second surge, the main glacier split into 6 segments due to

245 differential ablation, and the terminus of the lowest segment of the glacier was at 2950 m a.s.l. The terminus of the lowest

246 segment was about 2980 m a.s.l in 1969 as shown by the Corona reconnaissance satellite images (Kääb et al., 2021). The

247 terminus of the lowest part of the glacier had probably been at 2950 m a.s.l before 13 April 1984 when an ice mass of 80000

248 m² detached at 3700 m a.s.l and traveled horizontally 150 m (Zhang, 1992). After that, no glacier surges or detachments were

249 recorded, but small-scale mountain torrent or debris flows occurred almost yearly (Zhang and Shen, 2011). At present, the

250 glacier terminus is about 3770 m a.s.l.

设置了格式: 字体: (中文) + 中文正文 (宋体), (中文) 简体中文(中国大陆)

域代码已更改

域代码已更改

域代码已更改

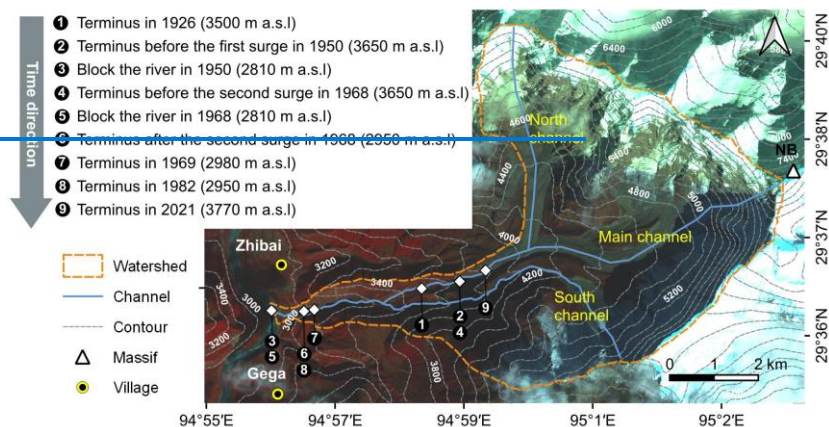


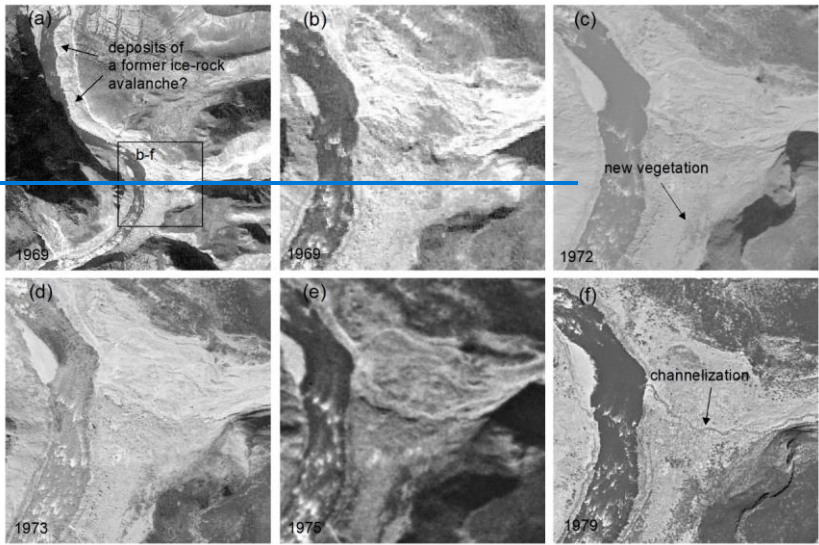
Figure 3: Variations of the Zelonglung main glacier terminus from 1926 to 2021. (The base image is taken from Planet satellite).

4.2.1 Multi-periodic glacial debris flows

Glacier surges or ice-rock avalanches can be transformed into debris flows that deliver massive amounts of sediment into the river or deposit on the alluvial fan. Four large-magnitude debris flows were triggered accompanied by the glacier instability events occurred in 1950, 1968, 1973, and 1984 (Zhang, 1992; Hu et al., 2020). From the 1972 and 1973 images, it is observed that fresh debris deposits inundated the north part of the fan and did not go beyond the 1968 accumulation zone (Fig. 43). The same lobes and deposition boundary indicate that the so-called 1973 event mentioned by Peng et al. (2022) Peng et al. (2022) likely happened in 1972. The magnitude of the 1950 event is perhaps more significant than that of the 1968 event. According to Zhang (1992), the detached glacier in 1950 climbed over the ~80 meters lateral moraine on the north at an elevation 4000 m and traveled downstream along the Zhibai gully (Fig. 1c and Fig. 54). Based on the erosional scar photo on the lateral moraine (Zhang, 1992) and the 2022 UAV photo, the residual depositional area of the 1950 event in the upstream gully is ~65,000 m² (Fig. 54). Although the glacier detachment happened in Zelunglung in 1950, most of the sediment deposited in the Zhibai channel and its alluvial fan. Fine sediment from the catchment can be quickly transported downstream by river flows, but most coarse sediment is still left on the bank or the alluvial fans.

设置了格式: 字体: 加粗

266



267

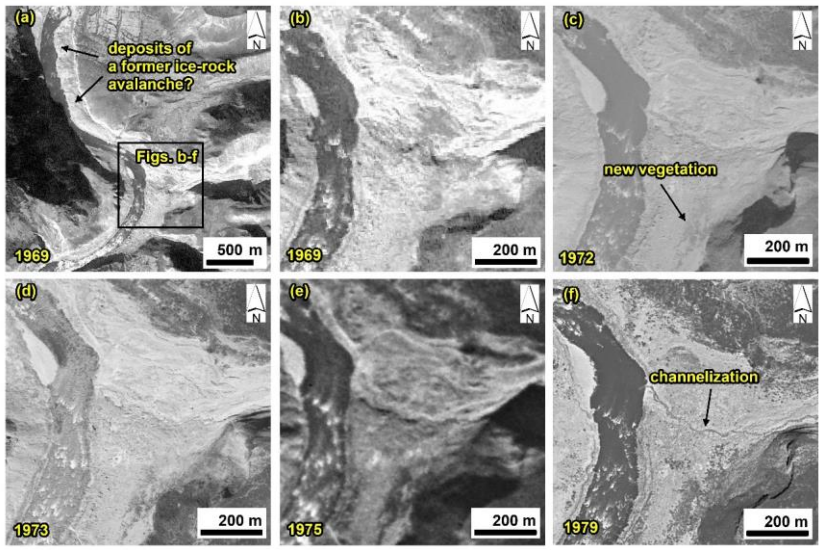


Figure 43: Variations of the Zelunglung alluvial fan during 1969 – 1979. The images are taken from Keyhole reconnaissance satellites (<https://earthexplorer.usgs.gov/>).

There are two terraces on the banks of the main river along the confluences of the Zelunglung ravine and Zhibai gully (Fig. 6a5a). T1 and T2 terraces are ~10 m and ~150 m above the river level, respectively (Fig. 6b5b). The 1950 and 1968 events completely dammed the Yarlung Tsangpo (Zhang, 1992). Compared with the 1969 Keyhole image (Fig. 4a3a), it is likely that the T1 terrace is the residual dam of the 1968 event. The debris flows in the 1950 glacier surge event eroded the T2 terrace, which implies that the T2 terrace formed before 1950. The residual inundation area of the 1950 event is ~0.78 km² (Fig. 6a5a). If the magnitude is proportional to the inundation area, the flow magnitude of the 1950 event could be larger than that of the 1968 event.





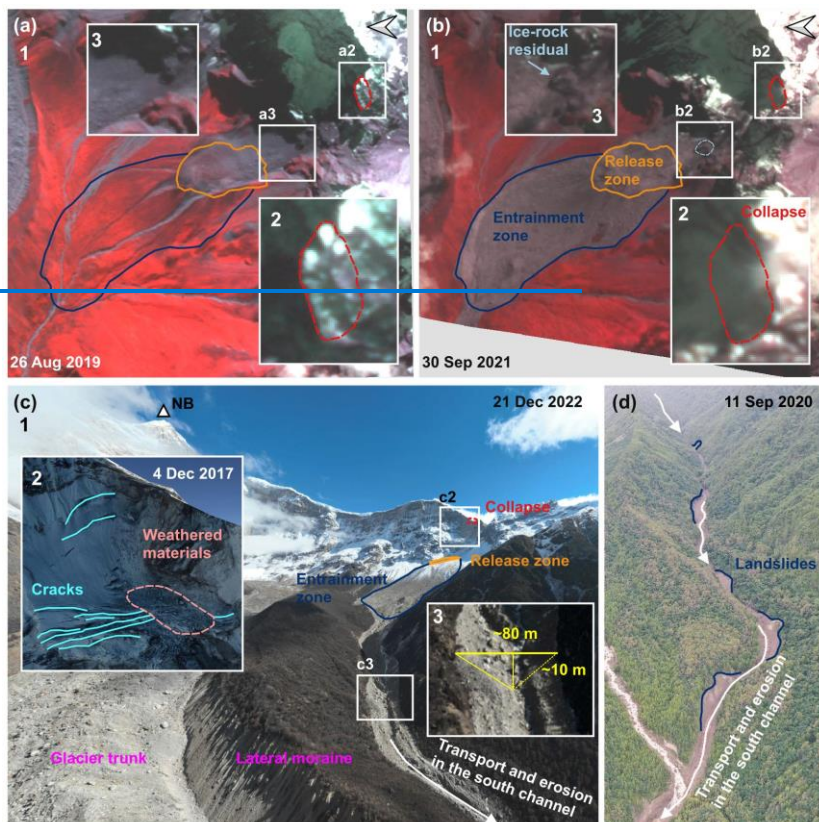
Figure 54: Aerial photo of the Zelunglung main channel on December 21, 2022, and the old deposits in Zhibai gully left by the 1950 event (the view angle direction is denoted by green arrow in figure 1c the camera faces to downstream, and the dashed rectangle indicates the location of Figure 6b5b).





Figure 65: Two terraces on the banks of the main river. (a) Century Space's satellite image on 9 February 2021. (b) Picture of the terraces on the opposite bank of the Zelunglung taken on 8 September 2020. (T1 and T2 represent the terraces formed in two different periods. The green arrow denotes the view angle direction of figure b)

An ice-rock avalanche triggered the recently documented glacial debris flow on Sep. 10, 2020. The 2020 ice-rock avalanche initiated on the top ridge of the south branch at an elevation of 5500 m. The scar area of initiated ice and rock was $1.35 \times 10^4 \text{ m}^2$ on the upper cliff (Figs. 7a6a-b). The initiated volume is estimated to be $7.0 \times 10^4 \text{ m}^3$ by using the bedrock landslide area-volume empirical relationship ($V = \alpha A^\gamma$; $\alpha = 0.186$, $\gamma = 1.35$) (Larsen et al., 2010). In the Google image on December 4, 2017 (Fig. 76-c2), it can be seen that there is a protruding rock mass on the cliff below the unstable ice-rock block. The rock mass develops many lateral cracks, and the top is covered with fresh, weathered materials, indicating freezing severe weathering. The fallen ice-rock block partially disintegrated and impacted colluvial deposits on steep hillslope below the cliff at elevations 4570–4800 m, forming a muddy fresh area of 0.134 km^2 (Fig. 7b6b). This area is often covered by snow and ice, and the ice-snow melting water easily infiltrates into the debris-ice mixtures. Once the slope material was entrained into the mass flow, such a nearly saturated mixture could quickly turn into a debris flow. Peng et al. (2022) estimated a debris loss of 1.14 Mm^3 in the scarp area except for the initiated ice and rock. But they mistake the hillslope below the cliff as the source area of the event. It is noted that there is an ice-rock residual of $\sim 7.14 \times 10^3 \text{ m}^2$ left under the cliff (Fig. 76-b3). That means the volume of the debris mass flowed downward into the south channel should include half of the initiated ice-rock mass and the debris loss of 1.14 Mm^3 . The entrained volume is at least 16 times the initiated volume.





303
304
305
306
307
308
309

310
311
312
313

that transformed from the entrained sediment and melting water exceeded the average water level of the south channel. The flow cross-section is ~ 80 m wide at the top and ~ 10 m high in the thalweg based on the UAV photo and OpenCycle topographic map (Fig. 76-c3). The peak discharge and frontal flow velocity reached 4700 m³/s and 11.4 m/s at the outlet (Peng et al., 2022). According to the description of local villagers, the first debris flow surge arrived at Zelunglung's mouth at about 5:00 pm on September 10, and the second larger one arrived about one hour later. Two ice-rock avalanches with different volumes probably happened on the ridge and were the corresponding trigger of the downstream debris-flow surges. But it is more likely that there was only one ice-rock avalanche during the event, but a synchronization of the ice-rock impacts in the scarp area, and the channel blockage caused two debris-flow surges.

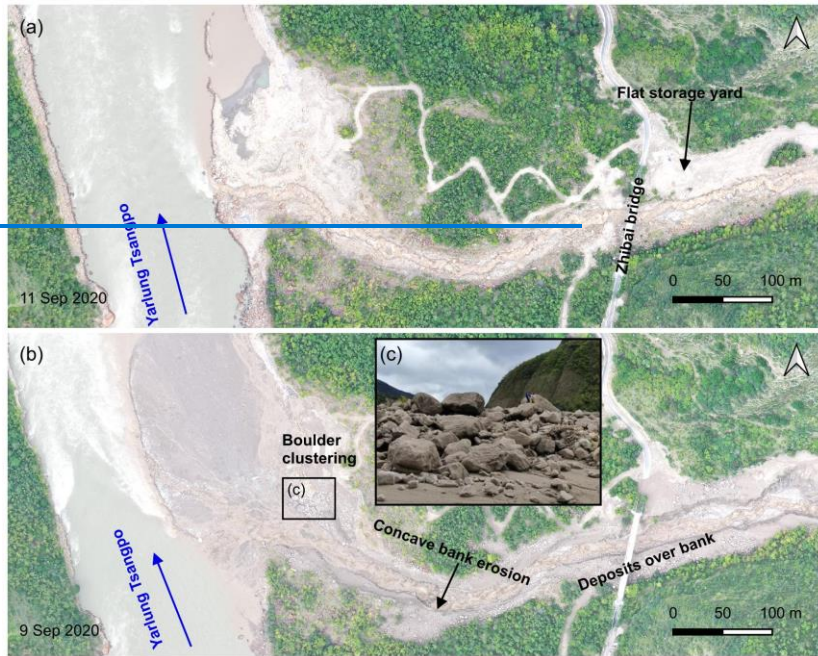
4.3.2 Sediment characteristics of the 2020 event

4.3.2.1 Difference between the initiation and the downstream areas

Periglacial debris flows can transport rocks or boulders not only in midstream steep channels but also in gentle downstream channels or alluvial fans. The sediment transportation capacity of the flows depends on flow hydrodynamics, grain composition, and topographic conditions. The 2020 Zelunglung event provides first-hand information for examining such sediment characteristics of the flows. Next, we present on-site data such as the size distribution of coarse grains, their impact, and erosion. The field evidence shows some features of periglacial debris-flow transportation that differ from fluvial transport.

There is a big difference between the sediment composition in the source and depositional areas. The initiated ice-rock debris and colluvial deposits on steep hillslopes consisted of angular rocks of various sizes. However, we observe that the deposits in the downstream areas are sub-rounded stones, and the downstream banks and channel bed are composed of sands and boulders up to several meters in diameter (Fig. 87). That means most of the angular rocks resided in the upslope or upstream channel and did not move downward. The angularity of the fragmented rocks reduced their mobility, and the attenuated overland flow had less transport capacity. The large sub-rounded or sub-angular boulders in the lower reaches came from the middle of the downstream reaches. We guess that grain segregation happened initially, and only fine parts of the ice-rock mass and melting water traveled downward the midstream. The resident angular rocks would be rounded gradually by the periglacial stream and transported downward by the subsequent floods or debris flows. The transportation mode of coarse grains is a kind of "Relay-race style", one event by one event.

Numerous boulders were on the channel and banks before the 2020 event, as seen from the aerial photo on 9 September 2020 (Fig. 8a7a). The in situ boulders were mobilized by the upstream flows and reorganized spatially. The boulders were prone to move together on the flat banks such as a flat storage yard near the bridge and the fan middle (Fig. 8b7b). The slope and flow depth are critical for the boulder's transport. Interstitial slurry among the boulders could separate from the boulders when the debris flows moved on a gentle slope or spread over an open fan (Fig. 8e7c). The interstitial slurry provided buoyancy for the boulders and reduced resistance between them and the bed. Once there was no interstitial slurry, the boulders quickly stopped.



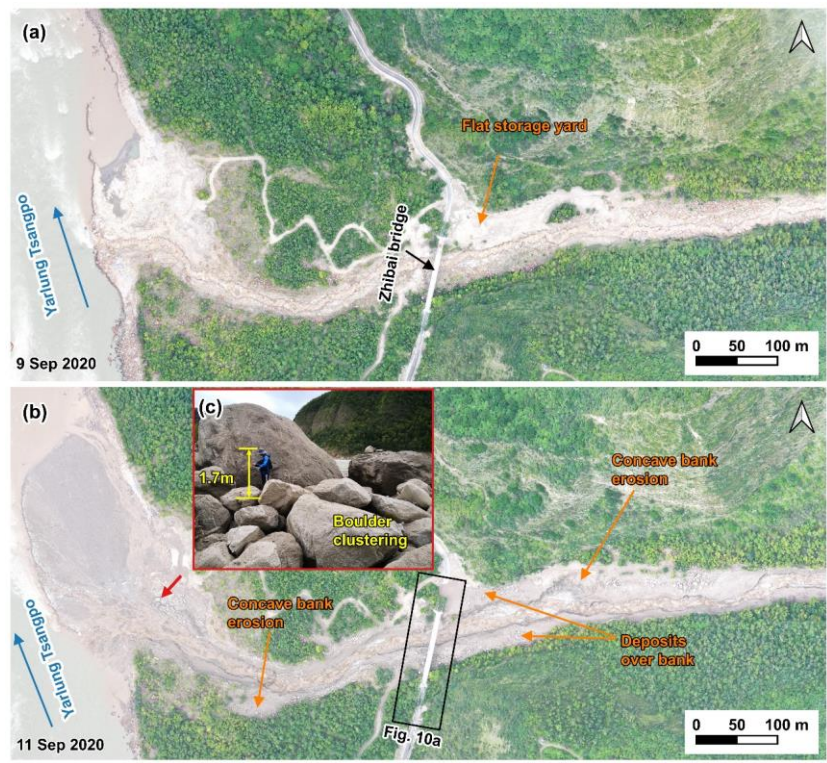
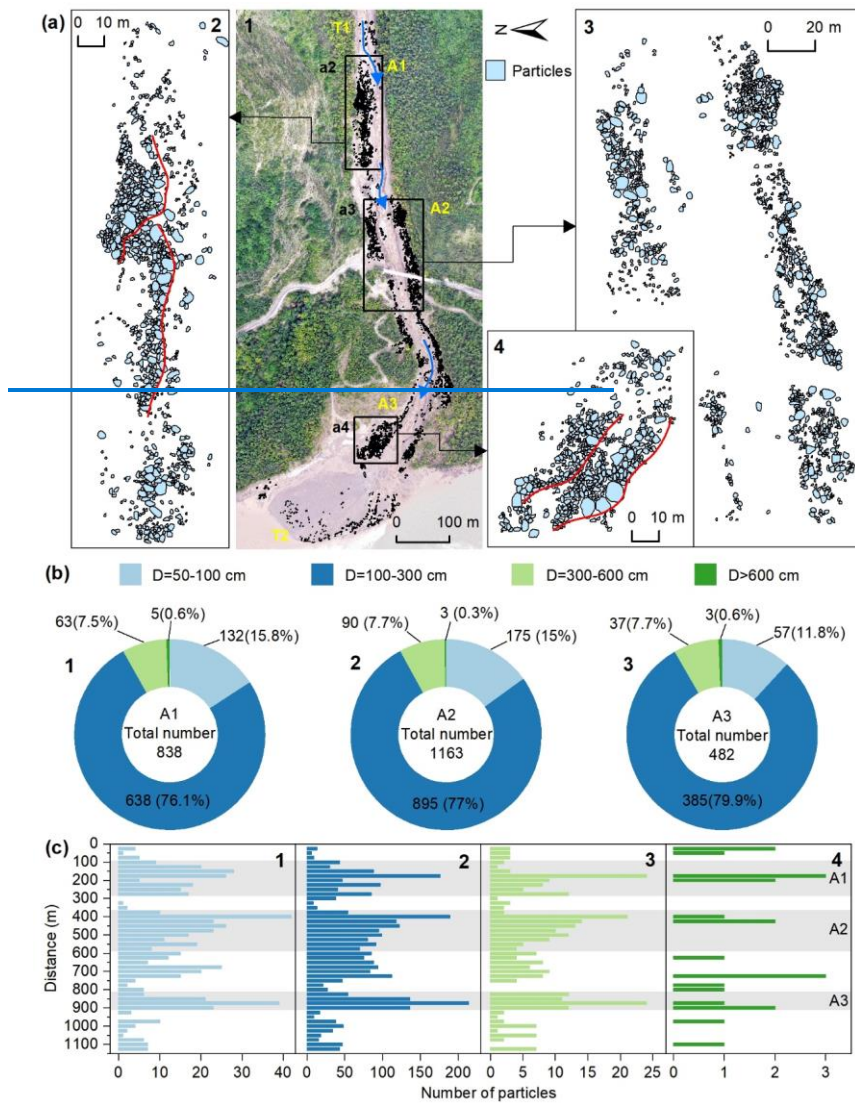


Figure 87: Comparison of pre-and post-event aerial photos on the downstream channel and alluvial fan. (a) the UAV photo on 9 September 2020; (b) the UAV photo on 11 September 2020; (c) On-site picture of the boulder clustering on 11 September 2020 (the man's height is 1.7 m; the camera angle direction is denoted by red arrow in figure b).

4.3.2.2 Grain-size distribution of coarse particles > 50 cm

In the downstream channel, with an average gradient of 13.8%, a relatively high velocity (11.4 m/s) enabled the flows to mobilize boulders of 5.0 meters in diameter (Costa, 1983). An 1125 m long straight reach from the first bend upstream of the bridge to the edge of the alluvial fan was chosen. Coarse particles > 50 cm on the deposition surface were visually interpreted from the orthophotos with a resolution of 0.17 m on September 11, 2020, after the debris-flow event. The long axis of the equivalent ellipse of these particles represents the particle size. Due to the limitation of resolution, only coarse particles with a long axis larger than 50 cm were counted (Fig. 98). A total of 3943 coarse particles were identified and divided into four size

357 ranges of 50-100, 100-300, 300-600 and >600 cm. Spatial statistics of these particles were made every 25 m along the central
358 flow line, and then 45 segments were divided.



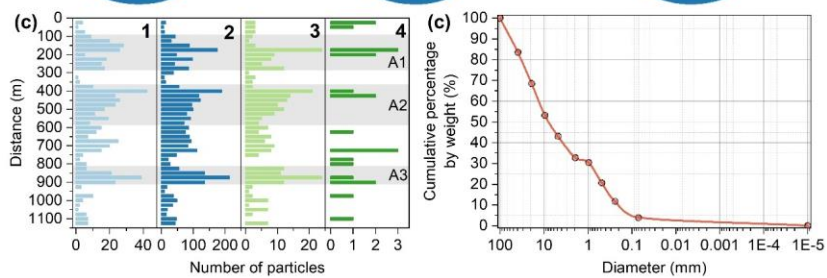
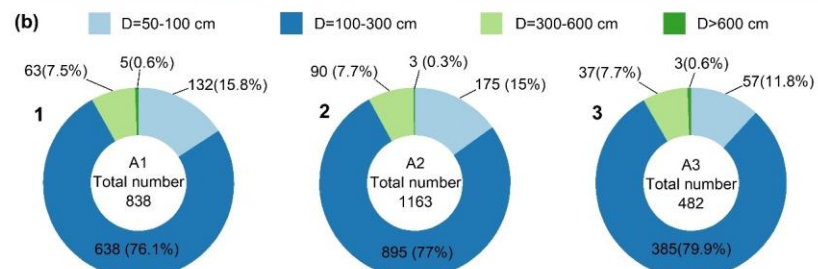
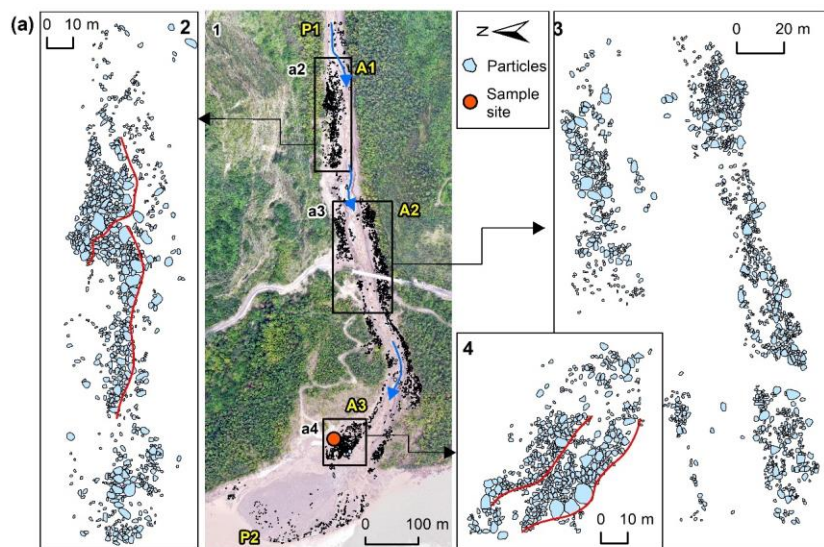


Figure 98: Distribution of the grain size coarse particles on the sediment surface. (a) The distribution of coarse particles along the channel and alluvial fan. T1-P1 and T2-P2 are the start and end points represent the places where the count starts and ends, respectively. A1-A3 are the three main deposition sites. The blue arrow is the direction of the debris flows. The bottom image is an orthographic image taken by a drone on September 10, 2020. The locations of the enlarged regions (a2)-(a4) are shown as black boxes. (a2)-(a4) enlarged region over the three main deposition sites A1-A3. Panels (b1)-(b3) show the counts of four groups of the particles in the three main deposition sites A1-A3. Panels (c1)-(c4) show the counts of four groups of the particles in the 45 segments along the channel from P1 to P2. Particles with diameters of 50-100 cm, 100-300 cm, 300-600 cm, and particles larger than 600 cm in panels b-c are shown in light blue, blue, light green, and green. (d) Cumulative grain size distribution of the on-site sample with size < 100 mm.

63% of the particles are concentrated in three zones A1, A2, A3 (Figs. 9a8a-b). The three zones are gentle banks or floodplains. The large stones easily slowed down when the flow depth and the velocity decreased on the edges of the debris flows. The composition of the particles in A1-A3 exhibits similar grain size distribution (Fig. 9b8b). The size of the most numerous particles is between 100 and 300 cm. The stones with the size > 600 cm are the least. The number of particles with 100-300 cm size accounts for 77.4% of the total. Likewise, the particles with sizes of 50-100 cm, 300-600 cm, and >600 cm, accounted for 14.3%, 7.7%, and 0.6% of the total, respectively. If the particle volume is estimated with the equivalent ellipsoid volume, i.e. $V = (4\pi abc) / 3$ (where a is major radius, b is short radius, c is polar radius and equal to b), the two groups of particles with the sizes of 100-300 cm and 300-600 cm have the largest volume.

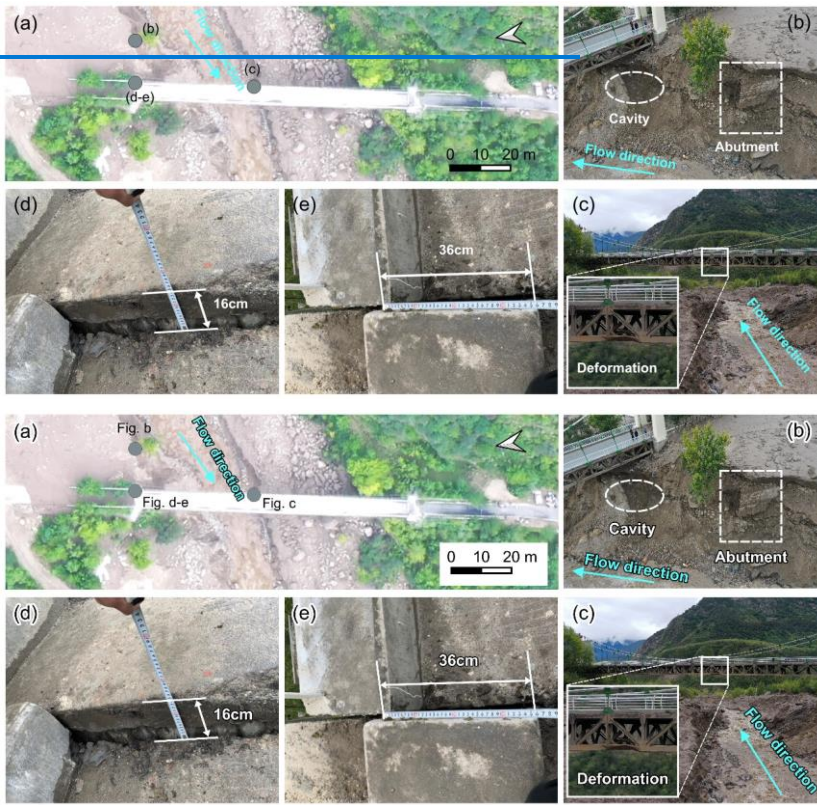
The spatial distribution of these particles in the 45 segments is shown in Figure 9e8c. The same four size ranges are used (50-100 cm, 100-300 cm, 300-600 cm, and > 600 cm). The particles with the first three sizes have three peaks in A1, A2, and A3 (Fig. 9e8c). The first peak is located on the right bank highland of A1. When the debris flows moved to A1, the flow depth was far higher than the channel depth. Many coarse particles were left on the highland. The second peak is located on both channel sides above Zhibai Bridge. When the debris flow enters the bend at a high speed, a large velocity difference will be generated on the concave-convex bank, i.e., the super-elevation effect (Chen et al., 2009). The debris flows produced the super-elevation effect when they moved to A2, a partially curved channel. Then, some coarse particles overflowed the channel and deposited on the A2 banks. The third peak is at the top of the alluvial fan. When the debris flows moved out the mouth and had no boundary constraint, the other coarse particles gradually deposited from the fan top to the fan edge due to loss of kinetic energy. In the A1 highland, the particle size decreased toward the outer edge of the channel (Fig. 98-a2), while the coarse particles in A2 were poorly sorted (Fig. 98-a3). In A3, the coarse particles on the surface show the parallel superposition of two depositional units, and the particle size of each depositional unit generally decreases toward the outer edge of the channel (Fig. 98-a4). It reflects the gradual accumulation of multiple debris-flow surges (Major, 1998; Sohn, 2000). The two depositional units may correspond to the two successive debris flow surges in Zelunglung at 5:00 pm and 6:00 pm.

4.32.3 Impact and erosion

Debris flows usually have steep coarse-grained surge fronts (snouts) and inter-surge watery flows (Mccoy et al., 2013; Yan et al., 2023). The periglacial debris flows in Zelunglung had similar spatial compositions. The granular flows (coarse-grained snouts) at the fronts exerted a powerful impact on obstacles, and the inter-surge watery flows or water-rich tails with relatively

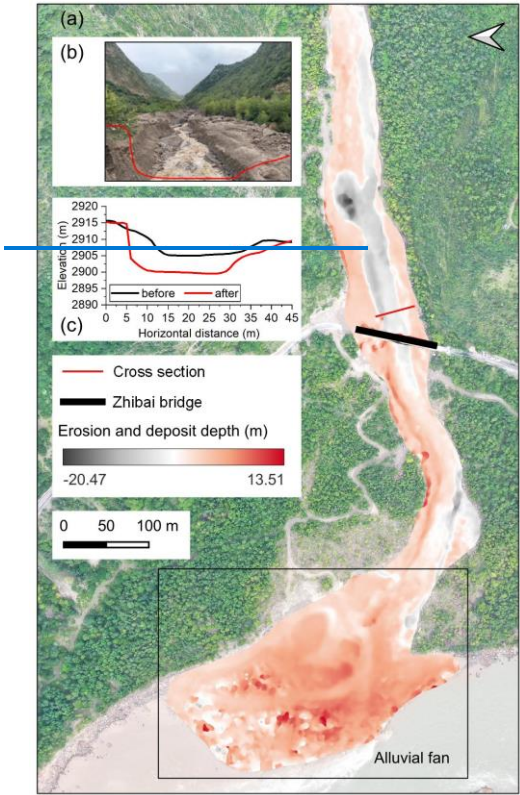
设置了格式: 字体: (中文) + 中文正文 (宋体)

low sediment concentration played critical roles in erosion. The Zelunglung debris flows had a very high content of coarse particles and wide distribution. The impact of the coarse particles witnessed by the damages of the Zhibai bridge, a 100m long cable bridge with a steel frame (Fig. 40a9a). The foundation of the bridge was exposed by the strong erosion capacity of the debris flows (Fig. 40b9b). The middle steel frame was intensely impacted by run-up boulders and highly deformed (Fig. 40c9c). The concrete bridge body displaced 16 cm in vertical direction and 36 cm in horizontal direction (Figs. 40d9d and 40e9e). The velocity of the largest boulder with a size of 9.9 m was 12.6 m s^{-1} , and the impact force of the largest boulder was estimated to be $3.64 \times 10^6 \text{ kN}$. The velocity of the debris flow at the selected cross section near the Zhibai bridge was 9.65 m/s , the peak value of debris-flow runoff was $1743.4 \text{ m}^3/\text{s}$ (Fig. 4110) (Li et al., 2023).



设置了格式: 字体: (中文) + 中文正文 (宋体)

Figure 409: Damages to the Zhibai Bridge caused by debris flows (photos taken on 11 Sep 2020). (a) The overview of Zhibai Bridge taken by UAV and the locations shown in photographs (b)-(e) taken with handheld cameras are shown in gray circles. (b) The photo of the damaged bridge foundation. (c) The photo of the damaged steel frame. (d) Photo of on-site measurements of the vertical displacement of the bridge. (e) Photo of on-site measurements of the horizontal displacement of the bridge.



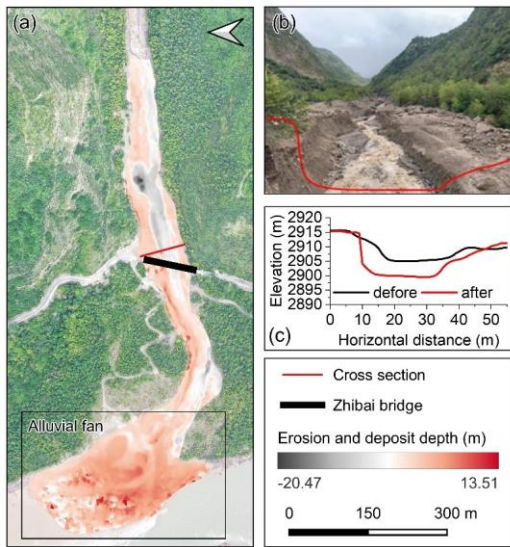


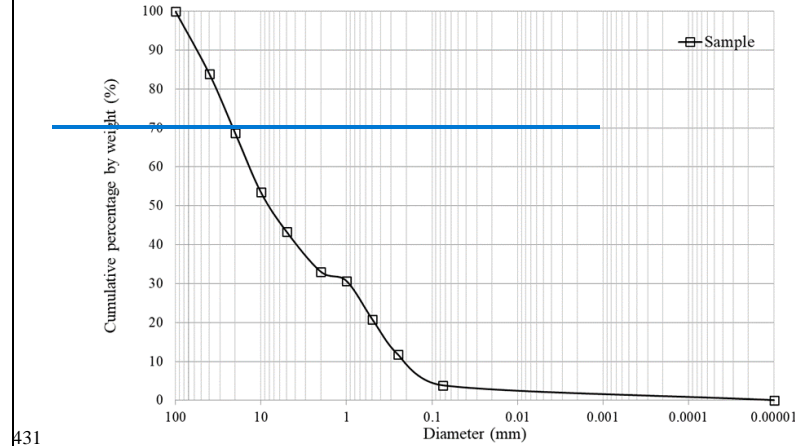
Figure 4410: Geomorphic changes of the channel and alluvial fan after the debris flows of 2020. (a) Erosion and deposit depth caused by the debris flows. The base map is taken by UAV on 10 Sep 2020. (b) Photo of the channel after the debris flows. The red line represents the cross-section next to the Zhibai Bridge (photo taken on 11 Sep 2020). (c) Cross-sections before (black) and after (red) the debris flows.

The watery flows were some kinds of dilute flows or hyper-concentrated flows. A vibrating sieve measured one sample taken from the debris-flow deposits with the size < 100 mm. The concentration of sediment finer than 0.075 mm is low, only 3.8% of the whole sample's mass (Fig. 428d). D50 and D90 of the sample are 8.3 mm and 62.9 mm, respectively, as linearly interpolated from the sieve-measured data. The field evidence shows that the debris flows strongly eroded the downstream channel. Comparing the drone-obtained Digital Surface Model (DSM) data before and after the 9.10 event, the maximum erosive depth was up to 20.47 m, and the mean erosive depth was 4.17 m (Fig. 4410a). Peng et al. (2022) numerically simulated the final erosion and deposition along the flow path. The maximum erosion depth was 7.41 m at the beginning of the downstream channel. We think the simulation underestimates the erosion depth because the final erosion accumulates several erosive watery flows. Lateral erosion happened nearly along the whole downstream channel. The channel width increased from 17 m to 33 m at 70 m upstream of the bridge. The lateral erosion exposed the bridge foundation, and a cavity formed below the pier (Fig. 40b9b). Concave bank erosion widened the channel by 14 m downstream. Based on the DSMsDoD, we estimated that at least $12.8 \times 10^4 \text{ m}^3$ ($\pm 1.85 \times 10^4 \text{ m}^3$) of debris was transported out of the catchment (Fig. 4410a). However, compared with the study of Peng et al. (2022), the true volume may be seriously underestimated because part of the

设置了格式: 字体: (中文) + 中文正文 (宋体)
带格式的: 正文

设置了格式: 字体: (默认) Times New Roman
设置了格式: 字体: (默认) Times New Roman, 上标
设置了格式: 字体: (默认) Times New Roman
设置了格式: 字体: (默认) Times New Roman, 上标
设置了格式: 字体: (默认) Times New Roman
设置了格式: 字体: 加粗
设置了格式: 字体: 加粗

429 sediment may be submerged ~~or carried away~~ by the Yarlung Tsangpo River, which is a bias caused by the difference in data
 430 acquisition time and DEM/DSM resolution.



431
 432 **Figure 12:** Cumulative grain size distribution of the on-site sample with size < 100 mm.

433 **5 Multi-periodic Sedimentation in the confluence**

434 Multi-periodic periglacial debris flows are strongly related to variations in the NVA of the alluvial fan. In practice, the NVA
 435 includes a fixed part of the area inundated by the river and then is larger than the debris-flow depositional or flooded area (**Fig.**
 436 **4311**). Technically, the NVA caused by the main river cannot be completely excluded from the total area. However, the river
 437 bank line was fixed from the 1980s to the 2010s when no periglacial debris flows happened (**Figs. 43b-11b and c**). So, it is
 438 reasonably assumed that the variation of the river water level has no significant influence on the NVA's change, and it
 439 represents the volume trend of the sediment transported by the debris flows.

440 From the Keyhole satellite image in 1969, the deposited debris from the 1968 event resided on the confluence and covered a
 441 2.5 km downstream reach of the Yarlung Tsangpo River from the junction (**Fig. 4a3a**) (**Kääb et al., 2021**). During 1969 – 1979,
 442 the area of the accumulated fan kept at about 0.28 km². The 1979 image shows vegetation gradually developed from the edge
 443 of the accumulation fan. A new channel developed along the 1972 deposition boundary across the middle of the fan (**Fig. 4f3f**).
 444 Since then, the area without vegetation cover has reduced to 0.048 km² in 2005 and kept a slight fluctuation from 1985 to
 445 2005. It indicates that only rainfall-induced small-scale flash floods or debris flows occurred during 1985-2005, which is
 446 confirmed by **Zhang and Shen (2011)**. The NVA increased slowly, with a slight variation from 2005-2019. In 2020, the NVA
 447 abruptly increased to 0.112 km² due to the ice-rock avalanche that happened on September 10 (**Fig. 4311**). The expansion of

NVA in 2020 demonstrates it is the most enormous debris flow event in the Zelunglung since 1972. At the same time, the river channel narrowed down by more than 60 meters compared to before. The multi-periodic sedimentation in the Zelunglung and Zhibai fans leads to rapids in this reach, forming a knickpoint before the river enters the Yarlung Grand Canyon.

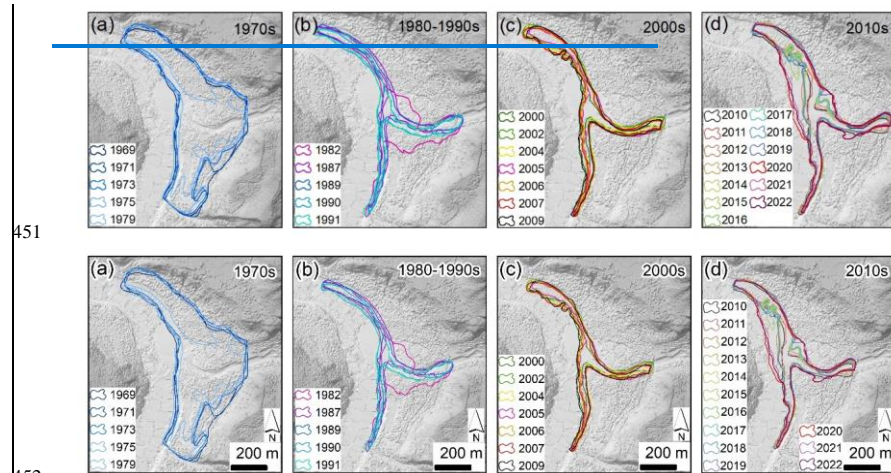


Figure 13: Evolution of the non-vegetated area in the Zelunglung alluvial fan from 1969 to 2022.

The data of seismic events since 1940 are collected from the United States Geological Survey (USGS) National Earthquake Center (NEIC) (<https://earthquake.usgs.gov/earthquakes/search/>) (Fig. 14a). It is observed that the four events in the Zelunglung in 1950, 1968, 1984, and 2020 were preceded by significant seismic activity. Nearly 30 earthquakes with $M_w \geq 4.5$ occurred within one year before the 2020 debris-flow event (10 September 2019 – 10 September 2020) whose epicentres are less than 200 km away from the Zelunglung. However, not all earthquakes influenced the instability of Zhelunglung's glaciers and hillslopes. Keefer (1984) presented an upper bound curve of maximum distance from epicenter to disrupted slide or fall (Fig. 15). Since 1940, only 12 earthquakes within a 420 km radius of ZLL fall below the bound curve, including the 1947 earthquake, the 1950 Assam earthquake and its aftershocks, the 1985 earthquake, and the 2017 Milin earthquake. If including the inundated area of $\sim 0.78 \text{ km}^2$ in 1950, the alluvial area disturbed by debris flows or floods decreased until 1990 and then kept at a low value before 2020 (Fig. 14d). If the 1950 debris flow event was directly triggered by the 1950 Assam earthquake, as Zhang (1992) suggested, the earthquake effect becomes negligible 40 years later. None of the other earthquakes significantly influenced the 1968 and 1984 debris-flow events, even if 13 earthquakes of $M_w > 5.1$ occurred in 1968 and 6 earthquakes of $M_w \geq 4.5$ occurred in 1984. The 2017 $M_w 6.4$ Milin earthquake, of which the epicenter is 24 km from the Zelunglung, probably has limited influence on its glacial activity because there is no report or sign on such glacier related

设置了格式: 字体: (中文) + 中文正文 (宋体)

468 hazards in the Zelonglung. However, there are direct proofs that the Milin earthquake caused the 2018 glacier surges and extra
469 large-scale debris flows in the Sedongpu (Hu et al., 2019; Zhang et al., 2022b), 25 km downstream of the Zelonglung.
470 Furthermore, we extracted the gridded mean values of annual mean air temperature, summer air temperature, annual
471 precipitation, and summer precipitation within the Zelonglung catchment during 1940–2021 from a 1-km monthly mean
472 temperature dataset for China (1901–2021) (Peng, 2019) and 1-km monthly precipitation dataset for China (1901–2021) (Peng,
473 2020), respectively (Fig. 14b and c). These data were validated using 496 independent meteorological observation points
474 (Peng et al., 2019). From 1940 to 2017, the annual mean and summer air temperatures at the Zelonglung kept relatively stable.
475 However, in 2018, there was a sudden and significant increase in the annual mean and summer air temperatures, with an
476 amplitude exceeding 2.5 °C. Since then, the temperatures have maintained at a high level. There has been no significant change
477 in annual and summer precipitation since 1940, but a slight decreasing trend has been observed since 2000. The rates of
478 atmospheric warming in the Tibetan and Himalayan regions are far higher than the general global warming rate since 1960,
479 which accelerates the rates of most glaciers shrinking and ice mass loss across the regions (Shugar et al., 2021; Zhang et al.,
480 2020). Undoubtedly, the on-going warming increases the frequency of such glacier-related slope failures. The number of
481 rockfalls per decade show a similar growing trend with mean annual air temperature in Chamonix, Mont Blanc massif, France
482 since 1934 (Deline et al., 2015). Shugar et al. (2021) suggested that the 2021 Chamoli catastrophic mass flow resulted from a
483 complex response of the geologic and topographic settings to regional climate change. Even though there is no direct
484 observation data of surface temperature in the Zelonglung highland, the three years of warming may change the thermal and
485 hydrological conditions of the Zelonglung's glaciers, such as the thermal regime at the rock-ice contact surface, melting rate
486 of the surface ice and snow, englacial drainage system, fostering the instability of ice-rock blocks on the top. Previous intense
487 seismic shaking could widen rock fractures and reduce the ice-rock strength. It is no doubt that the 2020 Zelonglung event is
488 the product of the interplay among geological movement, steep topography, and climate warming. However, based on the fact
489 that the trend of the 1990–2020 NVAs shows a good agreement with that of the air temperature in the same period, it is likely
490 that the 2020 event was driven by the recent local warming rather than by geological events such as the mass flow event in
491 1950.

域代码已更改

域代码已更改

域代码已更改

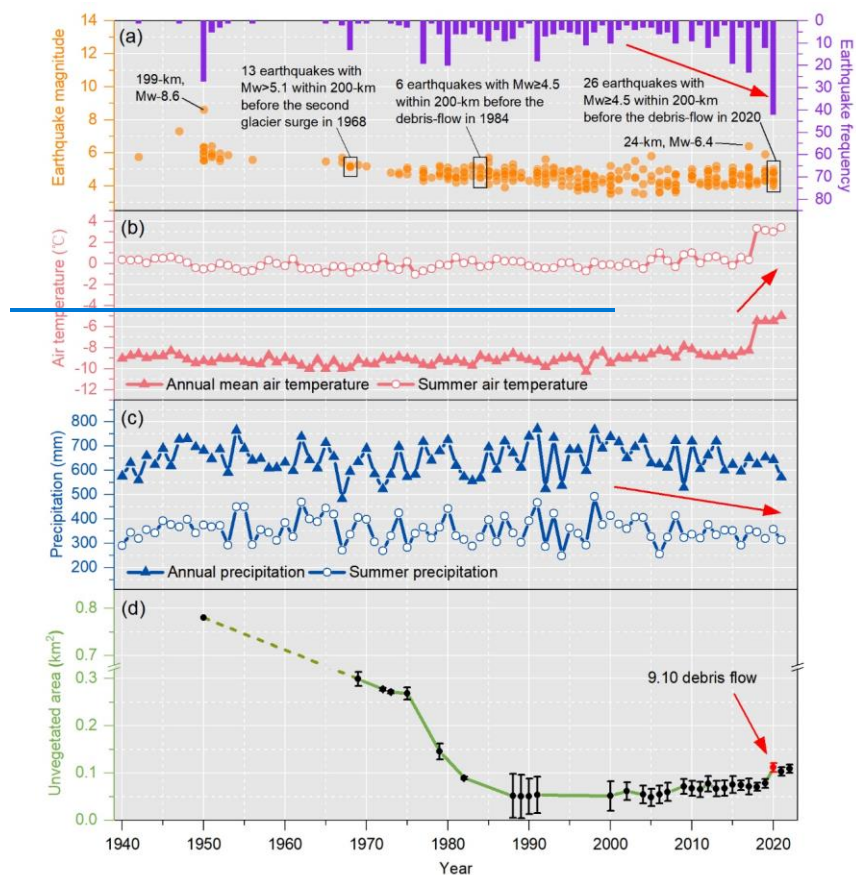


Figure 14: (a) Seismic events within a 200 km distance to the Zelunglung from 1940 to the present. (b) Changes in the annual mean and summer air temperatures in the Zelunglung from 1940 to the present. (c) Changes in the annual and summer precipitation in the Zelunglung from 1940 to the present. (d) Changes in the non-vegetated area of the Zelunglung alluvial fan from 1969 to the present (although the deposition of the 1950 event did not happen at the Zelunglung's outlet like the later events, we plot the NVA of the 1950 event as the starting point).

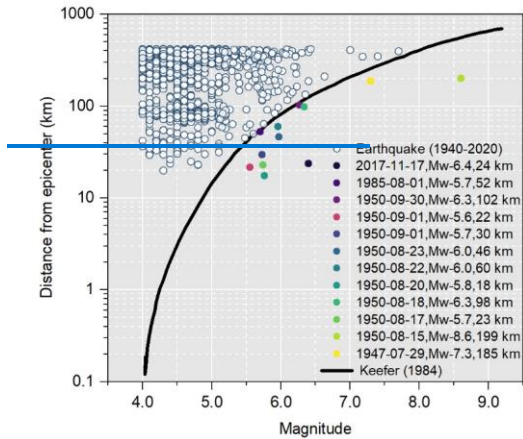


Figure 15: Distance from epicenters of the collected seismic events to the Zelunglung vs. the seismic magnitude (the black solid curve refers to Keefer (1984)).

6 Discussions

6.1 The dominant factor for debris flows and sediment yield

Strong ground vibrations caused by earthquakes can intensify cracking within the ice/rock mass, ultimately leading to the formation of substantial failure surfaces (Kilburn and Voight, 1998). Additional loading by earthquakes and coseismic-ice/rock avalanches could destruct the englacial conduit and subglacial drainage system. These changes can cause dynamic alterations to the glacier's thermal sensitivity, exacerbating its instability (Zhang et al., 2022b). As critical solid material sources, these highly active ice/rock masses caused by seismic disturbance are prone to avalanches, calving, detachment and remobilization to form glacial debris flows (Deng et al., 2017; Zhang et al., 2022b). The data of seismic events since 1940 are collected from the United States Geological Survey (USGS) National Earthquake Center (NEIC) (<https://earthquake.usgs.gov/earthquakes/search/>) (Fig. 1412a). It is observed that the four events in the Zelunglung in 1950, 1968, 1984, and 2020 were preceded by significant seismic activity. Nearly 30 earthquakes with $M_w > 4.5$ occurred within one year before the 2020 debris-flow event (10 September 2019 - 10 September 2020) whose epicentres are less than 200 km away from the Zelunglung. However, not all earthquakes influenced the instability of Zhelunglung's glaciers and hillslopes. Keefer (1984) presented an upper bound curve of maximum distance from epicenter to disrupted slide or fall (Fig. 1513). Since 1940, only 12 earthquakes within a 420-km radius of ZLL fall below the bound curve, including the 1947 earthquake, the 1950 Assam earthquake and its aftershocks, the 1985 earthquake, and the 2017 Milin earthquake. If including the inundated area of $\sim 0.78 \text{ km}^2$ in 1950, the alluvial area disturbed by debris flows or floods decreased until 1990 and then kept at a low value

518 before 2020 (Fig. 1412d). If the 1950 debris-flow event was directly triggered by the 1950 Assam earthquake, as Zhang (1992)
519 suggested, the earthquake effect becomes negligible 40 years later, as the understability of the glacier/materials caused by the
520 earthquake may have improved. Notably, the epicenter of the 1950 earthquake was located about 195 km away from the ZLL
521 basin. This seismic event also triggered a prolonged period of debris flow activity, persisting for decades, in Guxianggou,
522 approximately 50 kilometers northeast of the ZLL Valley (Du and Zhang, 1981). None of the other earthquakes significantly
523 influenced the 1968 and 1984 debris flow events, even if Although 13 earthquakes of $M_w > 5.1$ occurred in 1968 and 6
524 earthquakes of $M_w > 4.5$ occurred in 1984, the Keefer curve did not detect any of these seismic events. This suggests that
525 these earthquakes did not have a significant influence on the debris flow events of 1968 and 1984. The 2017 Mw 6.4 Milin
526 earthquake, of which the epicenter is 24 km from the Zelunglung, probably has limited influence on its glacial activity because
527 there is no report or sign on such glacier-related hazards in the Zelunglung. However, there are direct proofs that the Milin
528 earthquake caused the 2018 glacier surges and extra large-scale debris flows in the Sedongpu (Hu et al., 2019; Zhang et al.,
529 2022b), 25 km downstream of the Zelunglung.

城代码已更改

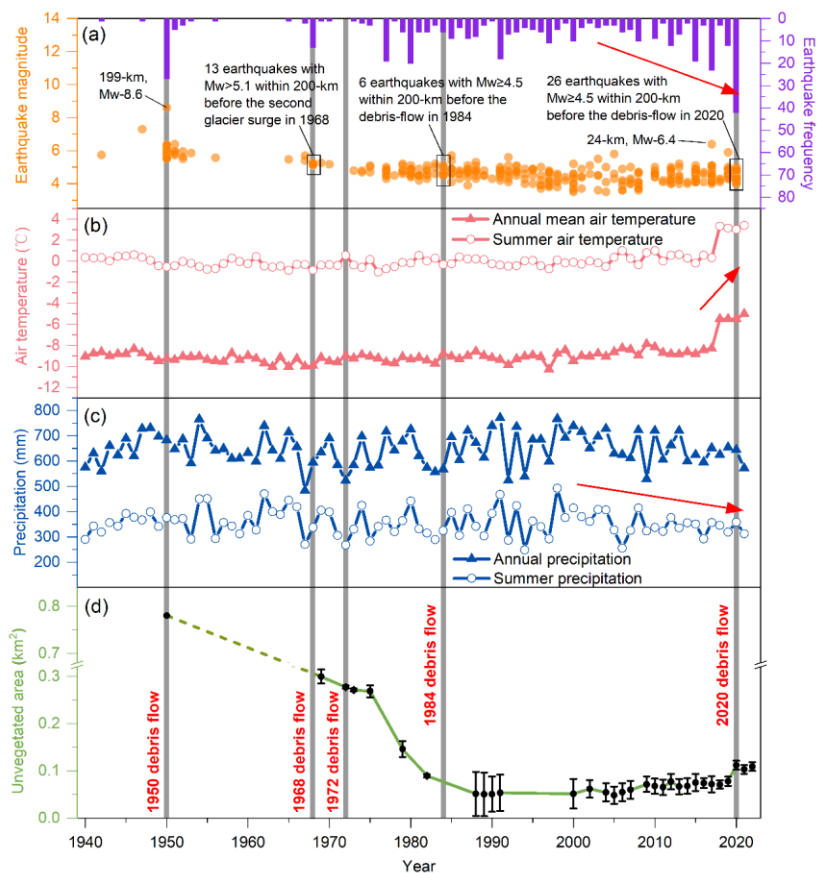


Figure 12: (a) Seismic events within a 200 km distance to the Zelunglung from 1940 to the present. (b) Changes in the annual mean and summer air temperatures in the Zelunglung from 1940 to the present. (c) Changes in the annual and summer precipitation in the Zelunglung from 1940 to the present. (d) Changes in the non-vegetated area of the Zelunglung alluvial fan from 1969 to the present (although the deposition of the 1950 event did not happen at the Zelunglung's outlet like the later events, we plot the NVA of the 1950 event as the starting point).

批注 [A1]: We have added the other 4 debris flows in Figure d for comparison.

设置了格式: 字体: (中文) Times New Roman

设置了格式: 字体: (中文) Times New Roman

带格式的: 题注

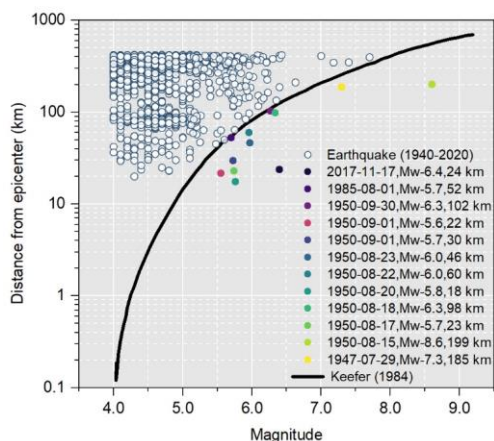


Figure 13: Distance from epicenters of the collected seismic events to the Zelunglung vs. the seismic magnitude (the black solid curve refers to Keefe (1984)).

带格式的: 题注

Furthermore, we extracted the gridded mean values of annual mean air temperature, summer air temperature, annual precipitation, and summer precipitation within the Zelunglung catchment during 1940 - 2021 from a 1-km monthly mean temperature dataset for China (1901-2021) (Peng, 2019) and 1-km monthly precipitation dataset for China (1901-2021) (Peng, 2020), respectively (Fig. 1412b and c). These data were validated using 496 independent meteorological observation points (Peng et al., 2019). From 1940 to 2017, the annual mean and summer air temperatures at the Zelunglung kept relatively stable. However, in 2018, there was a sudden and significant increase in the annual mean and summer air temperatures, with an amplitude exceeding 2.5 °C. Since then, the temperatures have maintained at a high level. There has been no significant change in annual and summer precipitation since 1940, but a slight decreasing trend has been observed since 2000. The rates of atmospheric warming in the Tibetan and Himalayan regions are far higher than the general global warming rate since 1960, which accelerates the rates of most glaciers shrinking and ice mass loss across the regions (Shugar et al., 2021; Zhang et al., 2020). Undoubtedly, the on-going warming increases the frequency of such glacier-related slope failures. The number of rockfalls per decade show a similar growing trend with mean annual air temperature in Chamonix, Mont Blanc massif, France since 1934 (Deline et al., 2015). Shugar et al. (2021) suggested that the 2021 Chamoli catastrophic mass flow resulted from a complex response of the geologic and topographic settings to regional climate change. Even though there is no direct observation data of surface temperature in the Zelunglung highland, the three years of warming may change the thermal and hydrological conditions of the Zelunglung's glaciers, such as the thermal regime at the rock-ice contact surface, melting rate of the surface ice and snow, englacial drainage system, fostering the instability of ice-rock blocks on the top. Previous intense seismic shaking could widen rock fractures and reduce the ice-rock strength. It is no doubt that the 2020 Zelunglung event is

域代码已更改

域代码已更改

the product of the interplay among geological movement, steep topography, and climate warming. However, based on the fact that the trend of the 1990-2020 NVAs shows a good agreement with that of the air temperature in the same period, it is likely that the 2020 event was driven by the recent local warming rather than by geological events such as the mass flow event in 1950.

It is evident that either earthquakes or climate change may increase the occurrence of periglacial debris flows and their sediment yield in southeastern Tibet (Du and Zhang, 1981; Deng et al., 2017; Wang et al., 2023). In the case of Zelunglung, the NVA closely related to the debris flows decreased until 1990 and slightly fluctuated around a low level until 2020. That means the effects of the 1950 earthquake were decaying; meanwhile, the local air temperature and precipitation had no significant variation until 2018. The response of hillslopes or glaciers to earthquakes is immediate. Had the 2017 Milin earthquake strongly impacted the glaciers in the Zelunglung, ice-rock failures would have happened a few months later. Like in the Sedongpu catchment. By contrast, the response of glaciers to warming will take longer. Meanwhile, approximately one month prior to the debris flow event, the maximum temperature recorded was 27°C, accompanied by a peak precipitation of merely 17.5mm. Notably, on the day the debris flow occurred, the steel bridge deck was dry, suggesting that the precipitation was very light (Peng et al., 2022). On the other hand, the magnitude of the warming-driven debris flows is smaller than that of the earthquake-driven. We believe the abrupt 2.5 °C warming in 2018-2020 is dominant in initiating the 2020 ice-rock avalanche.

6.1.2 The dominant factor and future risk

It is evident that either earthquakes or climate change increase the occurrence of periglacial debris flows and their sediment yield. In the case of Zelunglung, the NVA closely related to the debris flows decreased until 1990 and slightly fluctuated around a low level until 2020. That means the effects of the 1950 earthquake were decaying; meanwhile, the local air temperature and precipitation had no significant variation until 2018. The response of hillslopes or glaciers to earthquakes is immediate. Had the 2017 Milin earthquake strongly impacted the glaciers in the Zelunglung, ice-rock failures would have happened a few months later, like in the Sedongpu catchment. By contrast, the response of glaciers to warming will take longer. We believe the abrupt 2.5 °C warming in 2018-2020 is dominant in initiating the 2020 ice-rock avalanche.

On the other hand, the magnitude of the warming-driven debris flows is smaller than that of the earthquake-driven. Zhang et al. (2022a) predicted that cryosphere degradation driving the increasing sediment yield in cold regions is likely to shift from a temperature-dependent regime toward a rainfall-dependent one in the next century. But in tectonically active high-altitude areas, the temperature-dependent and the earthquake-dependent regimes will alternate in the future.

The period of the Zelunglung glacier surges is getting shorter. Zhang (1985) supposed that the surging cycle of the Zelunglung glacier was about 20 years. According to the latest research by Guillet et al. (2022), the Zelunglung glacier showed signs of surge in 2004, 2005, and 2006. Moreover, there are more obvious signs of a surge in 2016 (Fig. 1614). The interval between the last two surges is ten years, which shows that the surging cycle of the Zelunglung glacier may be decreasing, and the next

带格式的: 正文

large-scale surge may happen in the next ten years. Furthermore, changes in the speed of glacier movement can strongly impact channel side moraines or terminal moraines and lead to slope failures (Richardson and Reynolds, 2000). The potential ice collapse area in the formation area of the Zelunglung catchment is 2.4 km², the rock collapse area reaches 0.96 km², and the loose moraine accumulation reaches 5.2 km² (Liu et al., 2022; Li et al., 2021). However, the “9.10” debris flow was caused by a relatively small area of ice-rock collapses in the formation area, which is only the tip of the iceberg compared to the overall high-risk provenances in the formation area of the Zelunglung catchment. That means if intense earthquakes or extreme warming events happen not far away from the catchment, the risk of slope failures or glacier detachment on the steep slopes and ridges is high and huge amounts of sediment will be transported into the river by large-scale debris flows.

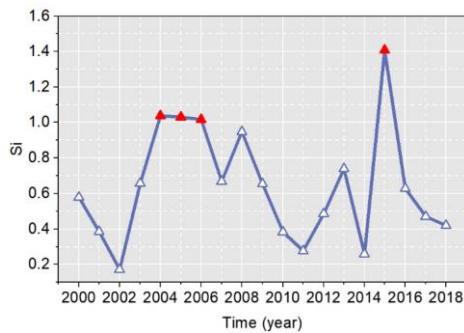


Figure 4614: Surge-index (S_i) of Zelunglung Glacier from 2000 to 2018. S_i is a quantitative index of the surge magnitude, calculated by the formula $S_i = \frac{IPR_i}{k \cdot V_0}$, where IPR_i is the inter-percentile range for year i , k is a threshold for surge identification, and V_0 is the error-weighted mean velocity for the study year. The years with $S_i > 1$ are marked with red triangles. (Data source: <https://doi.org/10.5281/zenodo.5524861> (Guillet et al., 2022)).

6.2.3 Effects on river geomorphology

The moraine and old deposits on both channel sides provided numerous boulders for debris flows. The number of coarse particles transported by the Zelunglung periglacial debris flows is very high, and there is no obvious particle sorting along the flow path. Most of the boulders are gneiss with high hardness, and the wearing and disintegration effects are not significant during the movement along the channel. Coarse particles are deposited on the platform at the bend and the top of the alluvial fan, where the channel suddenly widens. Such phenomenon demonstrates that the movement, deposition, and particle size distribution of the debris flow are not only related to the type of debris flow (Bardou et al., 2003) but also to topographic conditions (Zhou et al., 2019; Ghilardi et al., 2001).

The deposition of the “9.10” debris flow narrowed the Yarlung Tsangpo River at the mouth of the Zelunglung, and the river bed was significantly elevated. The river flow hardly transports the boulders on the alluvial fan. The peak discharge of the largest flood in the Yarlung Tsangpo recorded by the hydrologic station at Nuxia, 40 km upstream of the Zelunglung, is 16800

m³/s. The maximum size of the particles in such a flood is about 150 cm. The floods capable of moving the coarsest boulders (> 600 cm) deposited on the Zelunglung fan should be on the order of 10⁶ m³/s of peak discharge (Lang et al., 2013). Such high-magnitude floods in the Yarlung Tsangpo were caused by catastrophic breaching of landslide or glacial dams, e.g., several Quaternary megafloods in the middle and downstream of Yarlung Tsangpo (Hu et al., 2018; Yang et al., 2022; Liu et al., 2015), rather than caused by monsoonal runoffs. Modern outburst floods higher than 10⁵ m³/s only happened on the Yigong River, a downstream tributary of the Yarlung Tsangpo Gorge (Hu et al., 2021). Therefore, the time to evacuate the coarse sediments on the alluvial fan is two orders of magnitude of the recurrence period of periglacial debris flows. The long-lived protruding fan forms a knickpoint at the confluence. The repeated glacial and landslide dams in the margin of the Tibetan Plateau play significant roles in reducing the river incision into the plateau interior together with the moraine dams in the glaciation ages (Hu et al., 2021).

7 Conclusions

High-magnitude sediment evacuation by periglacial debris flows is a crucial surface process that links sediment yield from high-altitude slopes to river sediment transportation. The ongoing glacier degradation in the Himalayan mountains in response to recent earthquakes and climate change increases the frequency of the debris flows and their sediment volume. The Zelunglung catchment in the tectonically active eastern Himalayan syntaxis with a high uplift rate has recorded five periglacial debris flow events since 1950. These events delivered huge volumes of sediment into the Yarlung Tsangpo River. We examine the history of the five events and their sediment characteristics, especially the ice-rock-avalanche-triggered event in 2020, through field investigations and remote sensing interpretations. Some findings are concluded as follows:

- a) The periglacial debris flows have great capacities to erode channels, transport sediment, and impact obstacles. The maximum values of the erosion depth, the erosion width, and the impact force near the Zelunglung's outlet are about 20 m, 14 m, and 3.64×10⁶ kN, respectively, in the 2020 event. The debris flows transported a high concentration of coarse grains with the size > 50 cm. The 100-300 cm grains account for 77.4% of the coarse grains.
- b) Most of the angular rocks moved by the 2020 avalanche were not delivered downward further. The boulders transported by subsequent debris flows probably originated from the middle of the downstream reaches. The grain size segregation was not observed between the middle reach and the alluvial channel.
- c) The non-vegetated area of the Zelunglung's fan reduced from 0.78 km² in 1950 to 0.067 km² in 1990, and kept at a stable low value until 2020, indicating the influence of the 1950 earthquake on the debris-flow sediment transportation could last 40 years and keep at a stable low value until 2020. Compared with the 1999 Chi-chi earthquake and the 2008 Wenchuan earthquake in non-glaciated areas, the influence period of the 1950 earthquake is much longer.
- d) The seismic and local meteorological data show that the recent warming events drove the 2020 debris-flow event during 2018-2020. The surging cycle of Zelunglung's glaciers is getting short due to climate change. The correspondence between

the recent increases in the local air temperature and the NVA implies that the debris flow occurrences transfer from the tectonic-driven to the climatic-driven.

Acknowledgments. This research was funded by the Second Tibetan Plateau Scientific Expedition and Research Program (2019QZKK0902) and the National Natural Science Foundation of China (91747207, 41790434). MRG acknowledges the ‘ANSO Scholarship for Young Talents’ for his postgraduate study.

Data availability. All raw data can be provided by the corresponding authors upon request.

Author contributions. KHH conceptualized the study, interpreted the images, wrote and edited the manuscript. HL analyzed the data and wrote the manuscript draft. KHH, HL, SL, LW, XPZ, and BZ performed the field surveys. HL and MRG collected satellite and background data. LMZ provided constructive suggestions. All authors contributed to the preparation and editing of the paper.

Competing interests. The authors declare that they have no conflict of interests.

References

- Anaconda, P. I., Mackintosh, A., and Norton, K. P.: Hazardous processes and events from glacier and permafrost areas: lessons from the Chilean and Argentinean Andes, *Earth Surf Proc Land*, 40, 2-21, 10.1002/esp.3524, 2015.
- Bajracharya, S. R. and Mool, P.: Glaciers, glacial lakes and glacial lake outburst floods in the Mount Everest region, Nepal, *Ann Glaciol*, 50, 81-86, Doi 10.3189/172756410790595895, 2009.
- Bardou, E., Ancey, C., Bonnard, C., and Vulliet, L.: Classification of debris-flow deposits for hazard assessment in alpine areas, 3rd International Conference on Debris-Flow Hazards Mitigation, Davos, SWITZERLAND, 2003 Sep 10-12, WOS:000189451200068, 799-808, 2003.
- Chen, D., Xu, B., Yao, T., Guo, Z., Cui, P., Chen, F., Zhang, R., ZHANG, X., ZHANG, Y., and FAN, J.: Assessment of past, present and future environmental changes on the Tibetan Plateau, *Chinese Science Bulletin*, 60, 3025-3035, 2015.
- Chen, N., Yang, C., Li, Z., and He, j.: Research On the Relationship between the Calculation of Debris flow Velocity and Its Super Elevation in Bend, *Journal of Sichuan University. Engineering Science Edition*, 41, 165-171, 2009.
- Costa, J. E.: Paleohydraulic reconstruction of flash-flood peaks from boulder deposits in the colorado front range, *Geol. Soc. Am. Bull.*, 94, 986-1004, 10.1130/0016-7606(1983)94<986:Propf>2.0.Co;2, 1983.
- Cui, P., Zhou, G. G. D., Zhu, X. H., and Zhang, J. Q.: Scale amplification of natural debris flows caused by cascading landslide dam failures, *Geomorphology*, 182, 173-189, 10.1016/j.geomorph.2012.11.009, 2013.
- Cui, Y. L., Hu, J. H., Xu, C., Miao, H. B., and Zheng, J.: Landslides triggered by the 1970 Ms 7.7 Tonghai earthquake in Yunnan, China: an inventory, distribution characteristics, and tectonic significance, *J Mt. Sci.*, 19, 1633-1649, 10.1007/s11629-022-7321-x, 2022.
- Dadson, S. J., Hovius, N., Chen, H., Dade, W. B., Lin, J. C., Hsu, M. L., Lin, C. W., Horng, M. J., Chen, T. C., Milliman, J., and Stark, C. P.: Earthquake-triggered increase in sediment delivery from an active mountain belt, *Geology*, 32, 733-736, 10.1130/g20639.1, 2004.

Dai, L. X., Scaringi, G., Fan, X. M., Yunus, A. P., Liu-Zeng, J., Xu, Q., and Huang, R. Q.: Coseismic Debris Remains in the Orogen Despite a Decade of Enhanced Landsliding, *Geophysical Research Letters*, 48, 10.1029/2021gl095850, 2021.

David, R., Montgomery, and, Bernard, Hallet, and, Liu, Yuping, and and: Evidence for Holocene megafloods down the Tsangpo River gorge, southeastern Tibet, *Quaternary Res*, 2004.

Deline, P., Gruber, S., Delaloye, R., Fischer, L., Geertsema, M., Giardino, M., Hasler, A., Kirkbride, M., Krautblatter, M., Magnin, F., McColl, S., Ravel, L., and Schoeneich, P.: Chapter 15 - Ice Loss and Slope Stability in High-Mountain Regions, in: *Snow and Ice-Related Hazards, Risks, and Disasters*, edited by: Shroder, J. F., Haeberli, W., and Whiteman, C., Academic Press, Boston, 521-561, <https://doi.org/10.1016/B978-0-12-394849-6.00015-9>, 2015.

Deng, Mingfeng, Chen, Ningsheng, Liu, and Mei: Meteorological factors driving glacial till variation and the associated periglacial debris flows in Tianmo Valley, south-eastern Tibetan Plateau, *Natural hazards and earth system sciences*, 17, 345-356, 2017.

Ding, L., Zhong, D. L., Yin, A., Kapp, P., and Harrison, T. M.: Cenozoic structural and metamorphic evolution of the eastern Himalayan syntaxis (Namche Barwa), *Earth Planet Sc Lett*, 192, 423-438, Doi 10.1016/S0012-821x(01)00463-0, 2001.

Du, R. H. and Zhang, S. C.: Characteristics of glacial mud-flows in South-eastern Qinghai-Xizang Plateau, *Journal of Glaciology and Geocryology*, 10-16+81-82, 1981.

Evans, S. G. and Clague, J. J.: Recent climatic-change and catastrophic geomorphic processes in mountain environments, *Geomorphology*, 10, 107-128, 10.1016/0169-555x(94)90011-6, 1994.

Ghilardi, P., Natale, L., and Savi, F.: Modeling debris flow propagation and deposition, *Phys Chem Earth Pt C*, 26, 651-656, Doi 10.1016/S1464-1917(01)00063-0, 2001.

Guillet, G., King, O., Lv, M. Y., Ghuffar, S., Benn, D., Quincey, D., and Bolch, T.: A regionally resolved inventory of High Mountain Asia surge-type glaciers, derived from a multi-factor remote sensing approach, *Cryosphere*, 16, 603-623, 10.5194/tc-16-603-2022, 2022.

Haeberli, W., Whiteman, C. A., and Shroder, J. F.: *Snow and ice-related hazards, risks, and disasters*, Academic Press Waltham, MA2014.

Han, L. M. and Feng, Q. N.: Developmental characteristics and genetic mechanism of debris flow in Zelunglung Glacier, Nanga Bawa Peak, Inner Mongolia Science Technology & Economy, 58-59, 2018.

Hu, G., Yi, C. L., Liu, J. H., Wang, P., Zhang, J. F., Li, S. H., Li, D. H., Huang, J. W., Wang, H. Y., Zhang, A. M., Shi, L. F., and Shui, X. J.: Glacial advances and stability of the moraine dam on Mount Namcha Barwa since the Last Glacial Maximum, eastern Himalayan syntaxis, *Geomorphology*, 365, 14, 10.1016/j.geomorph.2020.107246, 2020.

Hu, H. P., Feng, J. L., and Chen, F.: Sedimentary records of a palaeo-lake in the middle Yarlung Tsangpo: Implications for terrace genesis and outburst flooding, *Quat. Sci. Rev.*, 192, 135-148, 10.1016/j.quascirev.2018.05.037, 2018.

Hu, K., Wu, C., Wei, L., Zhang, X., Zhang, Q., Liu, W., and Yanites, B. J.: Geomorphic effects of recurrent outburst superfloods in the Yigong River on the southeastern margin of Tibet, *Sci Rep*, 11, 10.1038/s41598-021-95194-1, 2021.

Hu, K. H., Zhang, X. P., You, Y., Hu, X. D., Liu, W. M., and Li, Y.: Landslides and dammed lakes triggered by the 2017 Ms6.9 Milin earthquake in the Tsangpo gorge, *Landslides*, 16, 993-1001, 10.1007/s10346-019-01168-w, 2019.

Huang, S. Y., Chen, Y. G., Burr, G. S., Jaiswal, M. K., Lin, Y. N., Yin, G. M., Liu, J. W., Zhao, S. J., and Cao, Z. Q.: Late Pleistocene sedimentary history of multiple glacially dammed lake episodes along the Yarlung-Tsangpo river, southeast Tibet, *Quaternary Res*, 82, 430-440, 10.1016/j.yqres.2014.06.001, 2014.

Huggel, C.: *Assessment of glacial hazards based on remote sensing and GIS modeling*, University of Zurich, Zürich2004.

Huggel, C., Haeberli, W., Kaab, A., Bieri, D., and Richardson, S.: An assessment procedure for glacial hazards in the Swiss Alps, *Can Geotech J*, 41, 1068-1083, 10.1139/t04-053, 2004.

Jia, H., Chen, F., and Pan, D.: Disaster chain analysis of avalanche and landslide and the river blocking dam of the Yarlung Zangbo River in Milin County of Tibet on 17 and 29 October 2018, *Int. J. Environ. Res. Public Health*, 16, 4707, 10.3390/ijerph16234707, 2019.

Kääb, A. and Girod, L.: Brief communication: Rapid ~ 335 x 10⁶ m³ bed erosion after detachment of the Sedongpu Glacier (Tibet), *Cryosphere*, 17, 2533-2541, 10.5194/tc-17-2533-2023, 2023.

Kääb, A., Jacquemart, M., Gilbert, A., Leinss, S., Girod, L., Huggel, C., Falaschi, D., Ugalde, F., Petrakov, D., and Chernomorets, S.: Sudden large-volume detachments of low-angle mountain glaciers—more frequent than thought?, *The Cryosphere*, 15, 1751-1785, 2021.

Kargel, J. S., Leonard, G. J., Shugar, D. H., Haritashya, U. K., Bevington, A., Fielding, E. J., Fujita, K., Geertsema, M., Miles, E. S., Steiner, J., Anderson, E., Bajracharya, S., Bawden, G. W., Breashears, D. F., Byers, A., Collins, B., Dhital, M. R., Donnellan, A., Evans, T. L., Geai, M. L., Glasscoe, M. T., Green, D., Gurung, D. R., Heijenk, R., Hilborn, A., Hudnut, K., Huyck, C., Immerzeel, W. W., Liming, J., Jibson, R., Kaab, A., Khanal, N. R., Kirschbaum, D., Kraaijenbrink, P. D., Lamsal, D., Shiyin, L., Mingyang, L., McKinney, D., Nahirnick, N. K., Zhuotong, N., Ojha, S., Olsenholler, J., Painter, T. H., Pleasants, M., Pratima, K. C., Yuan, Q. I., Raup, B. H., Regmi, D., Rounce, D. R., Sakai, A., Donghui, S., Shea, J. M., Shrestha, A. B., Shukla, A., Stumm, D., van der Kooij, M., Voss, K., Xin, W., Weihs, B., Wolfe, D., Lizong, W., Xiaojun, Y., Yoder, M. R., and Young, N.: Geomorphic and geologic controls of geohazards induced by Nepal's 2015 Gorkha earthquake, *Science*, 351, aac8353, 10.1126/science.aac8353, 2016.

Keefer, D. K.: Landslides caused by earthquakes, *Geol. Soc. Am. Bull.*, 95, 406-421, 10.1130/0016-7606(1984)95<406:Lcbe>2.0.Co;2, 1984.

Kilburn, C. R. and Voight, B.: Slow rock fracture as eruption precursor at Soufriere Hills volcano, Montserrat, *Geophysical Research Letters*, 25, 3665-3668, 10.1029/98gl01609, 1998.

Krautblatter, M., Funk, D., and Günzel, F. K.: Why permafrost rocks become unstable: a rock-ice-mechanical model in time and space, *Earth Surf Proc Land*, 38, 876-887, 10.1002/esp.3374, 2013.

Lang, K. A., Huntington, K. W., and Montgomery, D. R.: Erosion of the Tsangpo Gorge by megafloods, Eastern Himalaya, *Geology*, 41, 1003-1006, 10.1130/g34693.1, 2013.

Larsen, I. J., Montgomery, D. R., and Korup, O.: Landslide erosion controlled by hillslope material, *Nat. Geosci.*, 3, 247-251, 10.1038/ngeo776, 2010.

Li, H., HU, K. H., Zhang, X. P., Liu, S., and Wei, L.: Causes and Damage of the 2020 Periglacial Debris Flows at Zelunglung Catchment in the Eastern Syntaxis of Himalaya, *The XIV Congress of the International Association for Engineering Geology and the Environment*, Chengdu, China, 2023.

Li, J., Chu, H., Li, B., Gao, Y., Wang, M., Zhao, C., and Liu, X.: Analysis of development characteristics of high-elevation chain geological hazard in Zelongnong, Nyingchi, Tibet based on high resolution image and InSAR interpretation, *The Chinese Journal of Geological Hazard and Control*, 32, 9, 2021.

Li, W. L., Zhao, B., Xu, Q., Scaringi, G., Lu, H. Y., and Huang, R. Q.: More frequent glacier-rock avalanches in Sedongpu gully are blocking the Yarlung Zangbo River in eastern Tibet, *Landslides*, 19, 1-13, 10.1007/s10346-021-01798-z, 2022.

Li, Y., Yan, C., Hu, K., and Wei, L.: Variation of hazard areas of typical rainstorm debris flow alluvial fans, *Resources and Environment in the Yangtze Basin*, 26, 789-796, 2017.

Liu, M., Zhang, Y., Tian, S. F., Chen, N. S., Mahfuz, R., and Javed, I.: Effects of loose deposits on debris flow processes in the Aizi Valley, southwest China, *J Mt. Sci.*, 17, 156-172, 10.1007/s11629-019-5388-9, 2020.

Liu, W., Wang, M., Song, B., Yu, T., Huang, X., Jiang, Y., and Sun, Y.: Surveys and chain structure study of potential hazards of ice avalanches based on optical remote sensing technology: A case study of southeast Tibet, *Remote Sensing for Natural Resources*, 34, 265-276, 2022.

Liu, W. M., Lai, Z. P., Hu, K. H., Ge, Y. G., Cui, P., Zhang, X. G., and Liu, F.: Age and extent of a giant glacial-dammed lake at Yarlung Tsangpo gorge in the Tibetan Plateau, *Geomorphology*, 246, 370-376, 10.1016/j.geomorph.2015.06.034, 2015.

Liu, Y., Montgomery, D. R., Hallet, B., Tang, W., Zhang, J., and Zhang, X.: Quaternary Glacier Blocking Events at the Entrance of Yarlung Zangbo Great Canyon, Southeast Tibet, *Quaternary Sciences*, 26, 52-62. (in Chinese), 2006.

Major, J. J.: Pebble orientation on large, experimental debris-flow deposits, *Sediment Geol*, 117, 151-164, Doi 10.1016/S0037-0738(98)00014-1, 1998.

McCoy, S. W., Tucker, G. E., Kean, J. W., and Coe, J. A.: Field measurement of basal forces generated by erosive debris flows, *J. Geophys. Res.-Earth Surf.*, 118, 589-602, 10.1002/jgrf.20041, 2013.

Parker, R. N., Densmore, A. L., Rosser, N. J., de Michele, M., Li, Y., Huang, R. Q., Whadcoat, S., and Petley, D. N.: Mass wasting triggered by the 2008 Wenchuan earthquake is greater than orogenic growth, *Nat. Geosci.*, 4, 449-452, 10.1038/ngeo1154, 2011.

Peng, D. L., Zhang, L. M., Jiang, R. C., Zhang, S., Shen, P., Lu, W. J., and He, X.: Initiation mechanisms and dynamics of a debris flow originated from debris-ice mixture slope failure in southeast Tibet, China, *Eng. Geol.*, 307, 17, 10.1016/j.enggeo.2022.106783, 2022.

Peng, S. Z.: 1-km monthly mean temperature dataset for china (1901-2021), A Big Earth Data Platform for Three Poles [dataset], 10.11888/Meteoro.tpcd.270961, 2019.

Peng, S. Z.: 1-km monthly precipitation dataset for China (1901-2021), A Big Earth Data Platform for Three Poles [dataset], 10.5281/zenodo.3185722, 2020.

Peng, S. Z., Ding, Y. X., Liu, W. Z., and Li, Z.: 1 km monthly temperature and precipitation dataset for China from 1901 to 2017, *Earth Syst Sci Data*, 11, 1931–1946, 10.5194/essd-11-1931-2019, 2019.

Petrakov, D. A., Krylenko, I. V., Chernomorets, S. S., Tutubalina, O. V., Krylenko, I. N., and Shakhmina, M. S.: Debris flow hazard of glacial lakes in the Central Caucasus, 4th International Conference on Debris-Flow Hazards Mitigation - Mechanics, Prediction and Assessment, Chengdu, PEOPLES R CHINA, 2007

Sep 10-13, WOS:000267333300068, 703-+, 2007.

Richardson, S. D. and Reynolds, J. M.: An overview of glacial hazards in the Himalayas, *Quatern Int*, 65, 31-47, Doi 10.1016/S1040-6182(99)00035-X, 2000.

Shen, Y., Su, H., Wang, G., Mao, W., Wang, S., Han, P., Wang, N., and Li, Z.: The Responses of Glaciers and Snow Cover to Climate Change in Xinjiang (II): Hazards Effects, *Journal of Glaciology and Geocryology*, 35, 1355-1370, 10.1161/01.cir.45.6.1150, 2013.

Shugar, D. H., Jacquemart, M., Shean, D., Bhushan, S., Upadhyay, K., Sattar, A., Schwanghart, W., McBride, S., de Vries, M. V. W., Mergili, M., Emmer, A., Deschamps-Berger, C., McDonnell, M., Bhambri, R., Allen, S., Berthier, E., Carrivick, J. L., Clague, J. J., Dokukin, M., Dunning, S. A., Frey, H., Gascoin, S., Haritashya, U. K., Huggel, C., Kaab, A., Kargel, J. S., Kavanaugh, J. L., Lacroix, P., Petley, D., Rupper, S., Azam, M. F., Cook, S. J., Dimri, A. P., Eriksson, M., Farinotti, D., Fiddes, J., Gnyawali, K. R., Harrison, S., Jha, M., Koppes, M., Kumar, A., Leinss, S., Majeed, U., Mal, S., Muhuri, A., Noetzli, J., Paul, F., Rashid, I., Sain, K., Steiner, J., Ugalde, F., Watson, C. S., and Westoby, M. J.: A massive rock and ice avalanche caused the 2021 disaster at Chamoli, Indian Himalaya, *Science*, 373, 300-+, 10.1126/science.abh4455, 2021.

Sohn, Y. K.: Coarse-grained debris-flow deposits in the Miocene fan deltas, SE Korea: a scaling analysis, *Sediment Geol*, 130, 45-64, Doi 10.1016/S0037-0738(99)00099-8, 2000.

Tian, L. D., Yao, T. D., Gao, Y., Thompson, L., Mosley-Thompson, E., Muhammad, S., Zong, J. B., Wang, C., Jin, S. Q., and Li, Z. G.: Two glaciers collapse in western Tibet, *J Glaciol*, 63, 194-197, 10.1017/jog.2016.122, 2017.

Wang, J., Jin, Z. D., Hilton, R. G., Zhang, F., Densmore, A. L., Li, G., and West, A. J.: Controls on fluvial evacuation of sediment from earthquake-triggered landslides, *Geology*, 43, 115-118, 10.1130/g36157.1, 2015.

Wang, P., Wang, H., Hu, G., Qin, J., and Li, C.: A preliminary study on the development of dammed paleolakes in the Yarlung Tsangpo River basin, southeastern Tibet, *Earth Science Frontiers*, 28, 035-045, 2021.

Wang, Z., Hu, K. H., and Liu, S.: Classification and sediment estimation for debris flow-prone catchments in the Parlung Zangbo Basin on the southeastern Tibet, *Geomorphology*, 413, 14, 10.1016/j.geomorph.2022.108348, 2022.

Wang, Z., Ma, C., Hu, K., Liu, S., and Lyu, L.: Investigation of initiation conditions of periglacial debris flows in Sanggu watershed, Eastern Himalayas, Tibet Plateau (China), *Landslides*, 20, 813-827, 10.1007/s10346-022-02003-5, 2023.

Ward, F. K.: Explorations in south-eastern Tibet, *The Geographical Journal*, 67, 97-119, 1926.

Yan, Y., Tang, H., Hu, K. H., Turowski, J. M., and Wei, F. Q.: Deriving Debris-Flow Dynamics From Real-Time Impact-Force Measurements, *J. Geophys. Res.-Earth Surf.*, 128, 24, 10.1029/2022jf006715, 2023.

Yang, A. N., Wang, H., Liu, W. M., Hu, K. H., Liu, D. Z., Wu, C. H., and Hu, X. D.: Two megafloods in the middle reach of Yarlung Tsangpo River since Last-glacial period: Evidence from giant bars, *Glob. Planet. Change*, 208, 18, 10.1016/j.gloplacha.2021.103726, 2022.

Yu, G. A., Yao, W., Huang, H. Q., and Liu, Z.: Debris flows originating in the mountain cryosphere under a changing climate: A review, *Prog. Phys. Geogr.*, 45, 339-374, 2021.

Zhang, G. Q., Yao, T. D., Xie, H. J., Yang, K., Zhu, L. P., Shum, C. K., Bolch, T., Yi, S., Allen, S., Jiang, L. G., Chen, W. F., and Ke, C. Q.: Response of Tibetan Plateau lakes to climate change: Trends, patterns, and mechanisms, *Earth-Sci. Rev.*, 208, 22, 10.1016/j.earscirev.2020.103269, 2020.

Zhang, J. S. and Shen, X. J.: Debris-flow of Zelongnong Ravine in Tibet, *J Mt. Sci.*, 8, 535-543, 10.1007/s11629-011-2137-0, 2011.

Zhang, T., Li, D. F., East, A. E., Walling, D. E., Lane, S., Overeem, I., Beylich, A. A., Koppes, M., and Lu, X. X.: Warming-driven erosion and sediment transport in cold regions, *Nat Rev Earth Env*, 3, 832-851, 10.1038/s43017-022-00362-0, 2022a.

Zhang, W. J.: Some features of the surge glacier in the MT. Namjagbarwa, *Mountain Research*, 46-50, 1985.

Zhang, W. J.: Identification of glaciers with surge characteristics on the Tibetan Plateau, *Ann Glaciol*, 16, 168-172, 1992.

830 Zhang, X. P., Hu, K. H., Liu, S., Nie, Y., and Han, Y. Z.: Comprehensive interpretation of the Sedongpu glacier-related mass
831 flows in the eastern Himalayan syntaxis, *J Mt. Sci.*, 19, 2469-2486, 10.1007/s11629-022-7376-8, 2022b.
832 Zhou, G. G. D., Li, S., Song, D. R., Choi, C. E., and Chen, X. Q.: Depositional mechanisms and morphology of debris flow:
833 physical modelling, *Landslides*, 16, 315-332, 10.1007/s10346-018-1095-9, 2019.
834 Zhu, S., Wu, Z. H., Zhao, X. T., Li, J. P., and Wang, H.: Middle-Late Pleistocene Glacial Lakes in the Grand Canyon of the
835 Tsangpo River, Tibet, *Acta Geol Sin-Engl*, 86, 266-283, 10.1111/j.1755-6724.2012.00627.x, 2012.